



**HAL**  
open science

# Stationary fronts of the thermohaline circulation in the low-aspect-ratio limit

Laurence Fleury, Olivier Thual

► **To cite this version:**

Laurence Fleury, Olivier Thual. Stationary fronts of the thermohaline circulation in the low-aspect-ratio limit. *Journal of Fluid Mechanics*, 1997, 349, pp.117-147. 10.1017/S0022112097006678. hal-02864088

**HAL Id: hal-02864088**

**<https://amu.hal.science/hal-02864088v1>**

Submitted on 4 Sep 2024

**HAL** is a multi-disciplinary open access archive for the deposit and dissemination of scientific research documents, whether they are published or not. The documents may come from teaching and research institutions in France or abroad, or from public or private research centers.

L'archive ouverte pluridisciplinaire **HAL**, est destinée au dépôt et à la diffusion de documents scientifiques de niveau recherche, publiés ou non, émanant des établissements d'enseignement et de recherche français ou étrangers, des laboratoires publics ou privés.



Distributed under a Creative Commons Attribution - NonCommercial - NoDerivatives 4.0 International License

# Stationary fronts of the thermohaline circulation in the low-aspect-ratio limit

By LAURENCE FLEURY<sup>1</sup> AND OLIVIER THUAL<sup>2</sup>

<sup>1</sup>CERFACS, 42 Av. Coriolis, 31057 Toulouse Cedex, France

<sup>2</sup>INPT/ENSEEIH/IMFT, Av. du Pr. Soula, 31400 Toulouse, France

(Received 12 March 1996 and in revised form 31 October 1996)

A two-dimensional Boussinesq model of the thermohaline convection in a rectangular domain is forced at the top by a prescribed temperature and a prescribed salinity flux. The two forcings have opposite effects on the density field, which leads to the formation of fronts and multiple equilibria. Numerical results are interpreted through a comparison with the solutions of an asymptotic equation, derived in the limit of a shallow basin by Cessi & Young (1992). In order to explain the discrepancies between the numerical and the asymptotic solutions, we extend this asymptotic approach through a geometrical representation and a topological classification of the surface forcings. By comparing three forcings, we propose a global picture which gives clues to interpret the numerical solutions.

---

## 1. Introduction

The motion of a fluid layer forced by temperature and salinity gradients is called thermohaline convection. Rich dynamical behaviours result from the competition of the two buoyancy effects, particularly in the case where normal gradients are specified at the boundaries. In the present study, horizontal and vertical gradients result from buoyancy contrasts imposed at the free surface of a fluid layer, such as the ones that drive the thermohaline ocean circulation. When the density of the ocean is increased at the surface, the water column eventually becomes gravitationally unstable and convective overturning sets in. The heat and freshwater forcings at the ocean surface have opposite effects on the density field and, thus, on the deep convection. Cooling at high latitudes and heating at low latitudes favour sinking at the poles and rising at the equator, together with a surface transport from the equator to the poles. Inversely, freshwater input, through precipitation at high latitudes and strong net evaporation at low latitudes (except in a small belt of latitudes corresponding to the intertropical convergence zone, where precipitation is important) induces downwelling at the equator, upwelling at the poles and a surface transport from the poles to the equator. The actual circulation results from the two competing influences.

At present, deep water is mainly formed in subpolar regions, mostly in the northern North Atlantic and the Weddell Sea. The thermohaline circulation exhibits an asymmetric pattern in the Atlantic basin, with cross-equatorial southward deep flow and northward surface transport. In the North Pacific, no deep convection occurs. Paleoclimate records provide some evidence that, in the past, the thermohaline circulation has operated in another mode (Broecker, Peteet & Rind 1985) and that there have been very abrupt transitions between different regimes (Kennett & Stott 1991). Such changes in the thermohaline circulation would involve strong modifications in

the latitudinal distribution of heat, water and chemical tracers, and they are believed to have a large influence on the variability of climate.

The existence of multiple stable equilibria of the thermohaline circulation is supported by studies based on a hierarchy of models. First, Stommel (1961) solved the circulation between two boxes linked by hydraulic pipes, when one box is heated and salted (equatorial box) and the other cooled and freshened (polar box). Two stable solutions are obtained under the same forcing in a certain range of parameters. With models composed of three boxes (one equatorial and two polar ones), Rooth (1982) and Welander (1986) showed the existence of stable asymmetric states, composed of only one cross-equatorial cell, when the forcing is equatorially symmetric.

Using a three-dimensional ocean circulation model in an idealized geometry, Bryan (1986) observed a similar behaviour of the thermohaline circulation. Imposing a forcing symmetrical about the equator, two stable steady states are obtained, one of them being an asymmetric pole-to-pole circulation. Many authors have also observed multiple equilibria with realistic ocean models (Weaver *et al.* 1993) or coupled ocean–atmosphere models (Manabe & Stouffer 1988). Moreover, oscillations of the thermohaline circulation have been simulated on decadal, secular and millennial timescales (for a review of such results, see Weaver & Hughes 1992).

The mechanisms proposed to explain these phenomena occur essentially in the latitude–depth plane, except for decadal/interdecadal variability. Thus, it makes sense to use a two-dimensional model to study the thermohaline circulation. Indeed, multiple steady states (Marotzke, Welander & Willebrand 1988), secular oscillations (Winton & Sarachik 1993) and millennial variability (Marotzke 1990) have been observed through two-dimensional simulations.

In all these studies, the imposition of ‘mixed boundary conditions’ at the ocean surface appears to be necessary in order to observe multiple equilibria and oscillations. This means that the temperature and the salinity surface conditions should differ, so that the model cannot be formulated in terms of a single tracer (Welander 1986). This difference in the boundary conditions is consistent with reality: there is a strong feedback between the sea surface temperature and the surface heat flux to the ocean, while the flux of freshwater is independent of the sea surface salinity. In the two-box model of Stommel (1961), salinities and temperatures are restored to prescribed values, but the relaxation time is longer for the salinity than for the temperature. In two-dimensional and three-dimensional models, a restoring boundary condition is used for the temperature (flux proportional to a temperature deviation), while a flux condition is applied for the salinity. Since observations of such a flux are lacking, the model is spun-up with restoring boundary conditions for temperature and salinity. When an equilibrium is reached, the salinity flux is diagnosed and used afterwards as the surface condition. In some idealized studies (Thual & McWilliams 1992; Cessi & Young 1992; Dijkstra & Molemaker 1997), the restoring temperature boundary condition is replaced by a Dirichlet condition (prescribed temperature).

In box models (Stommel 1961), as in three-dimensional models (Weaver *et al.* 1993), the respective importance of the salinity and the temperature forcings has been pointed out as the controlling parameter in determining the existence of multiple regimes of the thermohaline circulation. The sensitivity to this parameter has been addressed precisely in some two-dimensional studies.

Thual & McWilliams (1992) studied a two-dimensional, non-rotating Boussinesq model in a rectangular pole-to-pole basin. The surface is forced by cosine salinity flux and cosine temperature. The control space is reduced to three parameters: the aspect ratio of the basin and the amplitudes of the surface forcings. For the same values of

the control parameters, three numerical equilibria can be identified in the numerical solutions (see figure 3). The thermally driven one (TH) is a two-celled circulation, symmetric about the equator, and exhibiting sinking at both poles and rising at the equator. The salinity-driven solution (SA) is a symmetric, two-celled circulation with sinking at the equator, and rising at both poles. The two pole-to-pole circulations (PP) have only one transequatorial cell, with sinking at one pole and rising at the other. The authors explored the parameter space and documented the catastrophe structure of the model. In the forcing amplitude plane, two cusps delimiting the domain of existence of multiple equilibria were found and the small-aspect-ratio limit was investigated.

Quon & Ghil (1992) analysed the bifurcation structure of the same two-dimensional Boussinesq model, applying a diagnosed flux. Again, multiple equilibria are obtained. When the salinity flux strength increases, the thermally dominated circulation is destabilized through a pitchfork bifurcation and asymmetric solutions can exist. At small aspect ratio, Quon & Ghil (1995) found a second bifurcation of Hopf type, leading from asymmetric steady solutions to oscillatory solutions.

Dijkstra & Molemaker (1997) studied the same two-dimensional Boussinesq model, with several types of mixed boundary conditions, using a path following technique. This enables them to catch stable and unstable solutions. When the Rayleigh number is strong enough, the bifurcation diagram presents two pitchfork bifurcations, leading to asymmetric states from a TH circulation or a SA solution. At large salt flux, oscillations are found as Hopf bifurcation of the PP circulation.

In a different approach, Cessi & Young (1992) performed an asymptotic expansion of the fluid model used by Thual & McWilliams (1992) in the limit of a thin layer. At the first order, the temperature and salinity are found to be vertically homogeneous. The two-dimensional model is reduced to a one-dimensional evolution equation for the vertically averaged salinity. This equation supports multiple solutions, corresponding to the minima of a Lyapounov functional. Since only one of the asymptotic solutions is globally defined in the basin, the authors had to add a higher-order diffusivity term and were eventually able to explain the catastrophe structure of the fluid model.

In the present paper, an interpretation of the Cessi & Young (1992) asymptotic analysis is proposed and validated through a comparison with numerical results obtained using different surface forcings. We denote as the *loop* case, the *straight* case and the *cubic* case three surface forcing functions inspired by physical considerations (warm and dry at the equator). These terms will be justified in §4.

The numerical results show multiple equilibria of the classical type TH/SA/PP, but also solutions exhibiting more than two cells. Separating two counter-rotating cells, a front exists where the latitudinal gradients are sharp. Within the boundary layers surrounding the front, the asymptotic scaling is not valid anymore. The asymptotic equation enables us to determine whether fronts can exist and to predict the topological structure of the solutions, following the surface forcing. The results obtained with the three surface forcings considered, associated solutions of which have different topologies, can be seen as the unfoldings of the same degenerate situation.

The outline of this paper is as follows. Model and numerical results for the different surface forcing functions are described in §2. The asymptotic expansion is recalled in §3. In §4, a geometric resolution of the asymptotic equation is explained and the topology of the asymptotic solutions is detailed for the three surface forcings studied. The comparison between numerical results and asymptotic predictions is presented in §5 for the *loop* case, in §6 for the *straight* case and in §7 for the *cubic* case. The last section presents conclusions and future directions of this study.

## 2. The thermohaline fluid model

### 2.1. The two-dimensional Boussinesq model

We consider a two-dimensional  $(y, z)$  layer of fluid in a rectangular basin of width  $L$  and depth  $d$ . Formulated in a non-rotating Cartesian frame, its evolution is governed by the Navier–Stokes equation, simplified by the Boussinesq approximation and conservation laws for heat and salt. The equations read

$$\left. \begin{aligned} \frac{\partial}{\partial t} \mathbf{u} + \mathbf{u} \cdot \nabla \mathbf{u} &= - \frac{\nabla p}{\rho_0} + B(T, S) \mathbf{e}_z + \nu \nabla^2 \mathbf{u}, \\ \nabla \cdot \mathbf{u} &= 0, \\ \frac{\partial}{\partial t} T + \mathbf{u} \cdot \nabla T &= \kappa_T \nabla^2 T, \\ \frac{\partial}{\partial t} S + \mathbf{u} \cdot \nabla S &= \kappa_S \nabla^2 S, \end{aligned} \right\} \quad (1)$$

where  $\mathbf{u}$  ( $v, w$ ) is the velocity vector field,  $p$  is the pressure field,  $\rho_0$  is an average value of the density  $\rho$ ,  $T$  and  $S$  are the temperature and salinity scalar fields and  $\mathbf{e}_z$  is the vertical unit vector. The dissipation parameters are the viscosity  $\nu$  and the thermal and saline diffusivities  $\kappa_T$  and  $\kappa_S$ . The buoyancy  $B(T, S)$  is given by the linear equation of state  $B(T, S) = -g \rho / \rho_0 = g (\gamma_T T - \gamma_S S)$ , where  $g$  is the gravitational acceleration and  $\gamma_T$  and  $-\gamma_S$  are the thermal and saline expansion coefficients.  $\nabla^2$  is the Laplacian operator.

From a geophysical point of view, the model can be thought of as a zonally averaged model of the world ocean. The modelling of the rotation can be included in the magnitude of the viscosity and diffusivity terms, as discussed in Marotzke *et al.* (1988) and Thual & McWilliams (1992). Moreover, Vellinga (1996) compared the dynamical behaviour of a two-dimensional non-rotating Boussinesq model with the zonally averaged model of Wright & Stocker (1991), which has a parametrization of rotation. He concluded that the two models are qualitatively similar. The transport equations for heat and salt seem to be more crucial in the understanding of thermohaline features than the details of the momentum budget.

### 2.2. Surface forcing and boundary conditions

Following Bryan (1986), the ocean surface is forced by mixed boundary conditions, i.e. a fixed temperature and a fixed salinity flux. This qualitative difference between the thermal and the saline forcings is chosen to reproduce the atmospheric influence on the ocean. Indeed, the strong feedback between oceanic and atmospheric temperatures leads to an equilibrium sea surface temperature, while the ocean salinity is forced by the water budget, composed of precipitation plus runoff minus evaporation, which is completely independent of the sea surface salinity. The forcing is chosen to be equatorially symmetric (i.e. symmetric to  $y = 0$ ) and is expressed as

$$T = \Delta T \mathcal{F}_T(y) \quad \text{and} \quad \frac{\partial}{\partial z} S = \frac{\Delta S}{d} \mathcal{F}_S(y) \quad \text{at} \quad z = 0, \quad (2)$$

where  $\Delta T$  and  $\Delta S$  are dimensional constants characterizing the magnitude of the forcings.  $\mathcal{F}_T(y)$  and  $\mathcal{F}_S(y)$  are non-dimensional functions, whose maximum is normalized to unity.

On the lateral sides ( $y = \pm L/2$ ) and the bottom ( $z = -d$ ) of the domain, no-flux boundary conditions are applied for the scalar fields:  $\partial T / \partial n = \partial S / \partial n = 0$ , where  $\partial / \partial n$  is the derivative in the direction normal to the boundary. For the velocity field,

free-slip boundary conditions are imposed on all the sides of the domain:  $w = 0$  and  $\partial v/\partial n = 0$  on horizontal boundaries ( $z = 0$  and  $z = -d$ ),  $v = 0$  and  $\partial w/\partial n = 0$  on vertical walls ( $y = \pm L/2$ ).

### 2.3. Dimensionless model

The model is non-dimensionalized using the following units:  $d$  for length in both spatial directions,  $2\pi d^3/L\kappa_T$  for time,  $\nu\kappa_T L^2/(4\pi^2 d^5 g\gamma_T)$  for temperature and  $\nu\kappa_T L^2/(4\pi^2 d^5 g\gamma_S)$  for salinity. The pressure is eliminated by introducing the streamfunction  $\Psi$ , related to the velocity by  $v = -\partial\Psi/\partial z$  and  $w = \partial\Psi/\partial y$ . With the notation  $J(f, g) = (\partial f/\partial y)(\partial g/\partial z) - (\partial f/\partial z)(\partial g/\partial y)$  for the Jacobian operator, the dimensionless equations for the conservation of vorticity and scalars are

$$\left. \begin{aligned} \frac{1}{k\sigma} \left[ \frac{\partial}{\partial t} \nabla^2 \Psi + J(\Psi, \nabla^2 \Psi) \right] &= \frac{1}{k} \frac{\partial}{\partial y} (T - S) + \nabla^4 \Psi, \\ \frac{1}{k} \left[ \frac{\partial}{\partial t} T + J(\Psi, T) \right] &= \nabla^2 T, \\ \frac{1}{k} \left[ \frac{\partial}{\partial t} S + J(\Psi, S) \right] &= Le \nabla^2 S, \end{aligned} \right\} \quad (3)$$

where  $\sigma = \nu/\kappa_T$  is the Prandtl number,  $Le = \kappa_S/\kappa_T$  is the Lewis number, and  $k = 2\pi d/L$  is the aspect ratio. The non-dimensional domain of motion is the box  $-\pi/k \leq y \leq \pi/k$  and  $-1 \leq z \leq 0$ .

In dimensionless form, the surface forcing is expressed as

$$T = a F_T(ky) \quad \text{and} \quad \frac{\partial}{\partial z} S = b F_S(ky) \quad \text{at} \quad z = 0, \quad (4)$$

where the non-dimensional magnitudes  $a = 4\pi^2 d^5 g\gamma_T \Delta T / (\nu\kappa_T L^2)$  and  $b = 4\pi^2 d^5 g\gamma_S \Delta S / (\nu\kappa_T L^2)$  are easily connectable to the thermal and saline Rayleigh numbers.  $F_T$  and  $F_S$  are such that  $F_T(ky) = \mathcal{F}_T(y)$  and  $F_S(ky) = \mathcal{F}_S(y)$ .

The streamfunction boundary conditions are  $\Psi = \partial^2 \Psi / \partial n^2 = 0$  on all the sides of the domain.

Thus, the model is controlled by five dimensionless parameters  $[a, b, k, \sigma, Le]$  and two non-dimensional functions  $[F_T(ky), F_S(ky)]$ . We will here consider the infinite Prandtl number limit  $\sigma \rightarrow \infty$  and the particular case  $Le = 1$ . Then, the model is only controlled by the aspect ratio and the surface forcing.

The choice  $\sigma \rightarrow \infty$  corresponds to an hypothesis in current use in climate studies (Maier-Reimer, Mikolajewicz & Hasselmann 1993). Indeed, for large-scale and long-term ocean studies, it is reasonable to linearize the momentum equation, and to diagnose the velocity field from the density field. The value  $Le = 1$  is chosen because there is no argument indicating why the large-scale heat and salt transports due to subgrid-scale processes should be different.

### 2.4. Numerical simulations

The equations are solved with the numerical code developed by Thual & McWilliams (1992). A finite difference scheme is used in the vertical direction and a Fourier decomposition is applied in the horizontal direction. We approximate the free-slip and no-flux lateral boundary conditions by considering a box of length  $2L$  and imposing either symmetry or asymmetry for the different fields, according to their nature. For most of the results presented here, the resolution counts 129 points

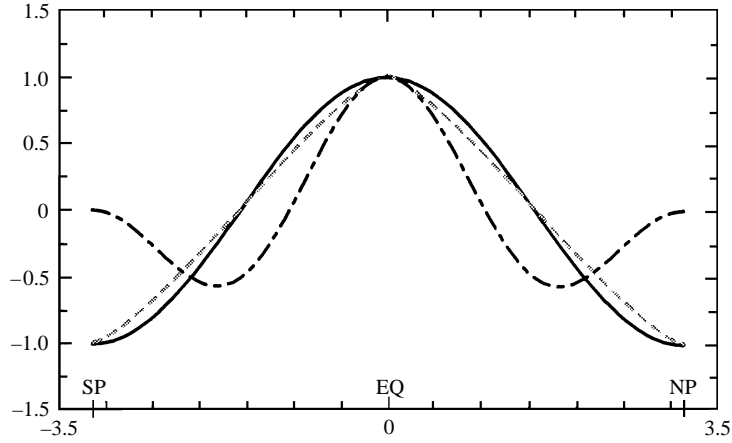


FIGURE 1. Surface forcing functions  $F_T(ky)$  and  $F_S(ky)$ ,  $ky \in [-\pi, \pi]$ : FT1 ( ——— ), FS2 ( - - - - ) and FT2 (grey dashed line).

equidistributed from  $y = -\pi/k$  to  $y = \pi/k$  in the horizontal direction and 17 vertical levels. The temporal scheme is a predictor-corrector one.

In this study, we consider two different functions for the surface temperature field: either

$$\text{FT1 : } F_T(ky) = \cos(ky), \quad (5)$$

or a slightly different forcing

$$\text{FT2 : } F_T(ky) = -2 \int_{-\pi/k}^y k \sin^{1/3}(ks) ds \Big/ \int_{-\pi/k}^0 k \sin^{1/3}(ks) ds. \quad (6)$$

In FT2, the bounds of the integral has been chosen such that the average of  $F_T(ky)$  on the domain is zero.

Two different profiles are used too for the surface salinity flux: either

$$\text{FS1 : } F_S(ky) = \cos(ky), \quad (7)$$

or

$$\text{FS2 : } F_S(ky) = [\cos(ky) + \cos(2ky)]/2. \quad (8)$$

The functions  $F_T(ky)$  and  $F_S(ky)$  are displayed in figure 1. They have been chosen to capture the meridional structure of the sea surface temperature (hot at the equator and cold at the poles) and of the salinity flux (excess of freshwater, and thus deficit of salt, at high latitudes and strong salinity input due to the evaporation at the equator). The FS2 case is similar to the salt flux applied in some previous studies (Marotzke *et al.* 1988; Quon & Ghil 1992), where it was diagnosed from an equilibrium state obtained by prescribing temperature and salinity at the ocean surface.

We study here three sets of forcing: FT1 and FS2 (the *loop* case), FT1 and FS1 (the *straight* case) and FT2 and FS1 (the *cubic* case). The meanings of these names are explained in §4. In all three cases, multiple equilibria are found, i.e. competing equilibria at a given value of the parameters ( $a, b, k$ ). The values of the parameters ( $a, b, k$ ) used in the figures presented below have been chosen so that the solutions obtained are representative of the multiple equilibria generated by each forcing.

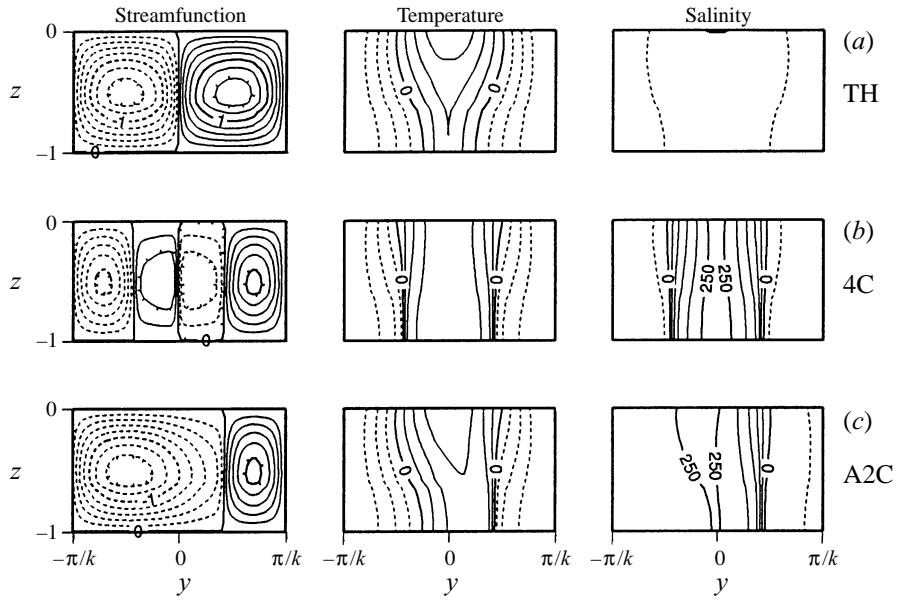


FIGURE 2. *Loop* case: three stable equilibria numerically observed with the surface forcing FT1 and FS2. The parameters are  $a = 200$ ,  $b = 40$ ,  $k = 0.2$ . Contour intervals are 0.2 for the streamfunction and 50 for the scalar fields  $T$  and  $S$ . (a) Thermally driven circulation TH, with sinking at both poles and rising at the equator. (b) Four-celled circulation 4C, with sinking at the poles and at the equator, and rising at the mid-hemispheres. (c) Asymmetric two-celled circulation A2C, with sinking at both poles and rising at the mid-latitude of the second hemisphere.

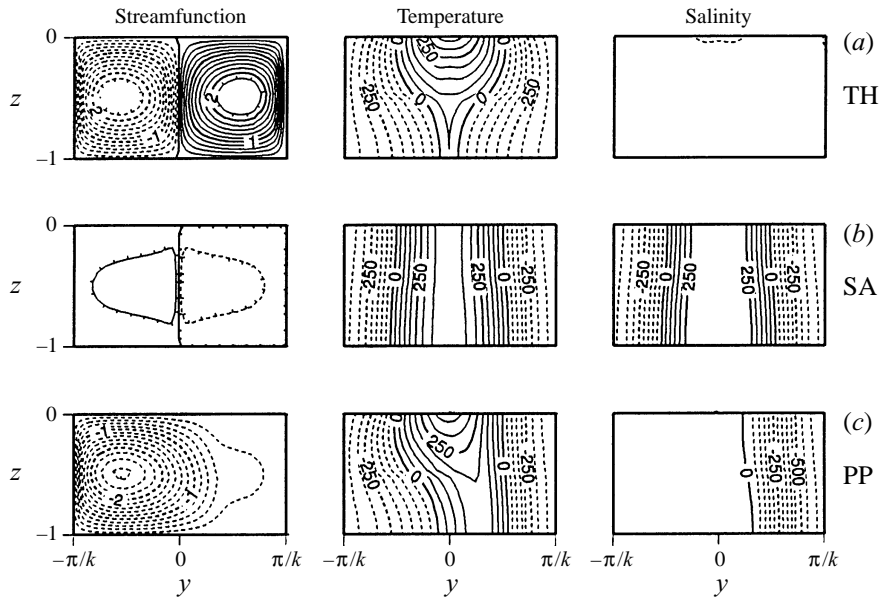


FIGURE 3. *Straight* case: three stable equilibria numerically observed with the surface forcing FT1 and FS1. The parameters are  $a = 380$ ,  $b = 30$ ,  $k = 0.2$ . Contour intervals are 0.2 for the streamfunction and 50 for the scalar fields  $T$  and  $S$ . (a) Thermally driven circulation TH, with sinking at both poles and rising at the equator. (b) Salinity-driven circulation SA, with sinking at the equator and rising at both poles. (c) Pole-to-pole circulation PP, with sinking at one pole and rising at the other.

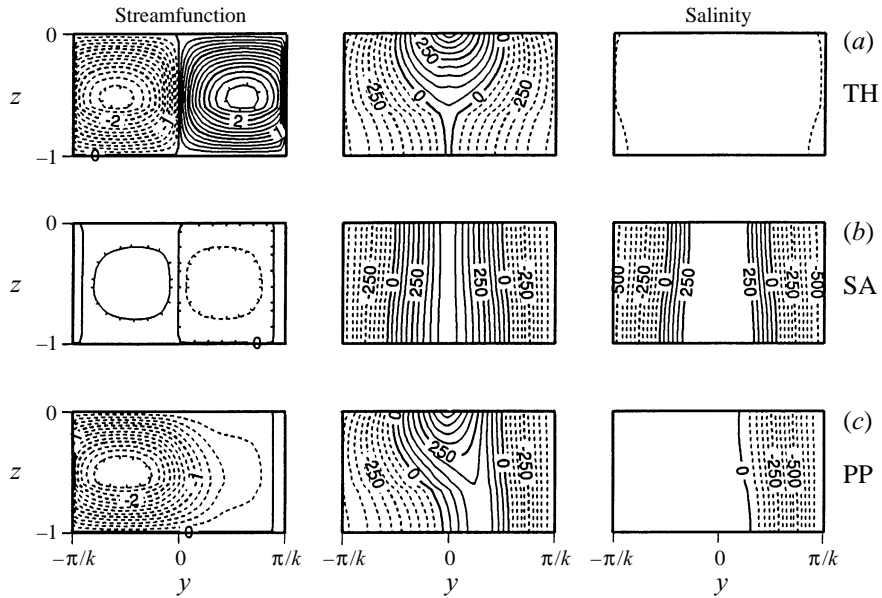


FIGURE 4. *Cubic* case: three stable equilibria numerically observed with the surface forcing FT2 and FS1. The parameters are  $a = 488$ ,  $b = 40$ ,  $k = 0.2$ . Contour intervals are 0.2 for the streamfunction and 50 for the scalar fields  $T$  and  $S$ . (a) Thermally driven circulation TH, with sinking at both poles and rising at the equator. (b) Salinity-driven circulation SA, with sinking at the equator and rising at high latitudes. Thin counter-rotating cells develop in the polar regions. (c) Pole-to-pole circulation PP, with sinking at one pole and, rising at the opposite high latitudes. A counter-rotating cell develops in the polar region close to the rising end of the principal cell.

Applying the forcing functions FT1 and FS2 (*loop*), stationary fronts separating two counter-rotating cells have been found. At the fronts, the different fields have very sharp latitudinal gradients. The front locations vary with the magnitudes of the applied forcing functions. Figure 2 provides an example of multiple equilibria existing in the *loop* case: there are a thermally driven circulation, denoted TH (figure 2a), a symmetric four-celled circulation, denoted 4C, with one front in the middle of each hemisphere (figure 2b), and an asymmetric two-celled solution, denoted A2C, with a single front at the middle of one hemisphere (figure 2c). A fourth equilibrium exists, which is the reflection of A2C with respect to the equator.

Using FT1 and FS1 (*straight*) as forcing functions, three kinds of circulations are obtained for the same set of parameters: a thermally driven circulation (TH, figure 3a), a salinity-driven circulation (SA, figure 3b) and two asymmetric pole-to-pole circulations (PP, figure 3c and its reflection with respect to the equator).

With FT2 and FS1 (*cubic*), the three previous types of circulations are again observed (TH is displayed in figure 4(a), SA in figure 4(b), and PP in figure 4(c)). Fronts located close to the lateral boundaries are found in the SA and PP cases. An explanation of their existence is given below. Note that boundary fronts can also develop with the *straight* forcing (FT1 and FS1).

In the three cases, the ‘superposition principle’ introduced by Thual & McWilliams (1992) can be observed: each hemisphere acts independently from the other one, and the asymmetric solutions are exactly obtained by adding two halves of the two different symmetric circulations.

### 3. Asymptotic expansion

In the limit of a small aspect ratio  $k \rightarrow 0$ , an asymptotic expansion of this model has been performed by Cessi & Young (1992). It is recalled here, using different notation for the purpose of the following sections.

#### 3.1. The asymptotic path

We consider the asymptotic path  $\epsilon \rightarrow 0$  in the control space, where  $a = \epsilon a_{(1)}$ ,  $b = \epsilon^3 b_{(3)}$  and  $k = \epsilon k_{(1)}$ . The fields are expanded in powers of  $\epsilon$ :

$$\left. \begin{aligned} \Psi(y, z, t) &= \epsilon \Psi_{(1)}(ky, z, \epsilon^2 kt) + \epsilon^2 \Psi_{(2)}(ky, z, \epsilon^2 kt) + \dots \\ T(y, z, t) &= \epsilon T_{(1)}(ky, z, \epsilon^2 kt) + \epsilon^2 T_{(2)}(ky, z, \epsilon^2 kt) + \dots \\ S(y, z, t) &= \epsilon S_{(1)}(ky, z, \epsilon^2 kt) + \epsilon^2 S_{(2)}(ky, z, \epsilon^2 kt) + \dots \end{aligned} \right\} \quad (9)$$

In addition to  $z$ , the independent variables will be denoted by  $\mathcal{Y} = ky$  and  $\mathcal{T} = \epsilon^2 kt$ .

#### 3.2. Expansion order by order

At the first order in  $\epsilon$ , the solutions are

$$\left. \begin{aligned} T_{(1)}(\mathcal{Y}, z, \mathcal{T}) &= a_{(1)} F_T(\mathcal{Y}), \\ S_{(1)}(\mathcal{Y}, z, \mathcal{T}) &= s_{(1)}(\mathcal{Y}, \mathcal{T}), \\ \Psi_{(1)}(\mathcal{Y}, z, \mathcal{T}) &= - \left[ a_{(1)} \frac{d}{d\mathcal{Y}} F_T(\mathcal{Y}) - \frac{\partial}{\partial \mathcal{Y}} s_{(1)}(\mathcal{Y}, \mathcal{T}) \right] P(z), \end{aligned} \right\} \quad (10)$$

where  $P(z) = (z^4 + 2z^3 - z)/24$  is the polynomial satisfying  $d^4 P/dz^4 = 1$  and the boundary conditions  $P = d^2 P/dz^2$  at  $z = 0$  and  $z = -1$ . The temperature and salinity fields are vertically homogeneous at the first order. The function  $s_{(1)}(\mathcal{Y}, \mathcal{T})$  is undetermined at this order.

At the second order, the solutions are

$$\left. \begin{aligned} T_{(2)}(\mathcal{Y}, z, \mathcal{T}) &= a_{(1)} \frac{d}{d\mathcal{Y}} F_T(\mathcal{Y}) \left[ a_{(1)} \frac{d}{d\mathcal{Y}} F_T(\mathcal{Y}) - \frac{\partial}{\partial \mathcal{Y}} s_{(1)}(\mathcal{Y}, \mathcal{T}) \right] Q(z), \\ S_{(2)}(\mathcal{Y}, z, \mathcal{T}) &= \frac{1}{Le} \frac{\partial}{\partial \mathcal{Y}} s_{(1)}(\mathcal{Y}, \mathcal{T}) \left[ a_{(1)} \frac{d}{d\mathcal{Y}} F_T(\mathcal{Y}) - \frac{\partial}{\partial \mathcal{Y}} s_{(1)}(\mathcal{Y}, \mathcal{T}) \right] Q(z), \end{aligned} \right\} \quad (11)$$

where  $Q(z) = (2z^5 + 5z^4 - 5z^2)/240$  is the polynomial which satisfies  $dQ/dz = P$  and the required boundary conditions for the temperature and the salinity. In the expression for  $S_{(2)}$ ,  $Q(z)$  could be replaced by  $Q(z) + C_q$ , where  $C_q$  is an arbitrary constant, because the compatibility condition is satisfied at this order. In particular, the choice  $C_q = 1/240$  ensures that the vertical average of  $S_{(2)}$  vanishes, and amounts to a definition of  $s_{(1)}(\mathcal{Y}, \mathcal{T})$  as the depth-averaged salinity. The temperature and salinity fields have the same vertical structure at this order. The expression for  $\Psi_{(2)}(\mathcal{Y}, z, \mathcal{T})$  can be calculated, but is not needed here.

At the third order in  $\epsilon$ , the compatibility condition comes from the salinity equation and reads

$$\frac{1}{Le} \frac{\partial}{\partial \mathcal{T}} s_{(1)} = b_{(3)} F_S + k_{(1)}^2 \frac{\partial^2}{\partial \mathcal{Y}^2} s_{(1)} + \frac{\partial}{\partial \mathcal{Y}} \left[ C^2 \left( a_{(1)} \frac{d}{d\mathcal{Y}} F_T - \frac{\partial}{\partial \mathcal{Y}} s_{(1)} \right)^2 \frac{\partial}{\partial \mathcal{Y}} s_{(1)} \right], \quad (12)$$

with

$$C^2 = \frac{1}{Le^2} \int_{-1}^0 P^2(z) dz = \frac{1}{Le^2} \frac{31}{24^2 \times 630} \sim 8.5 \times 10^{-5}.$$

This value of  $C^2$  differs from the one printed in Cessi & Young (1992).

### 3.3. Asymptotic equations

We introduce the following notation:

$$\left. \begin{aligned} \Theta(y, t) &= \epsilon \Theta_{(1)}(ky, \epsilon^2 kt) = \epsilon \frac{\partial}{\partial \mathcal{Y}} T_{(1)}(ky, z, \mathcal{T}), \\ \Sigma(y, t) &= \epsilon \Sigma_{(1)}(ky, \epsilon^2 kt) = \epsilon \frac{\partial}{\partial \mathcal{Y}} S_{(1)}(ky, z, \mathcal{T}), \end{aligned} \right\} \quad (13)$$

representative of the theoretical solution(s). With these definitions,  $\Theta(y, t)$  and  $\Sigma(y, t)$  are respectively the latitudinal temperature and salinity gradients.

Connected to the surface forcing, we define  $B(y)$  and  $\alpha(y)$  such that

$$\left. \begin{aligned} \frac{d}{dy} B(y) &= \epsilon^3 \frac{d}{d\mathcal{Y}} B_{(3)}(ky) = \epsilon^3 b_{(3)} F_S(ky), \\ \alpha(y) &= \epsilon \alpha_{(1)}(ky) = \epsilon a_{(1)} \frac{d}{d\mathcal{Y}} F_T(ky). \end{aligned} \right\} \quad (14)$$

In defining  $B(y)$  from  $F_S(\mathcal{Y})$ , we impose  $B = 0$  at the lateral boundaries, so that  $B(y)$  is the vertically averaged salinity flux due to the forcing. Indeed, the forcing cannot induce a non-zero horizontal salinity flux through the domain.

Taking the  $\mathcal{Y}$ -derivative of the compatibility equation (12) and introducing the notation above, the asymptotic system reads

$$\left. \begin{aligned} \Theta(y) &= \alpha(y), \\ \frac{k}{Le} \frac{\partial}{\partial t} \Sigma(y, t) &= \frac{\partial^2}{\partial y^2} \left\{ B(y) + k^2 \Sigma(y, t) + C^2 [\Theta(y) - \Sigma(y, t)]^2 \Sigma(y, t) \right\}. \end{aligned} \right\} \quad (15)$$

Moreover, the streamfunction at the first order is

$$\Psi(y, z, t) = [\Sigma(y, t) - \Theta(y)] P(z). \quad (16)$$

The asymptotic system can be reduced to

$$\frac{k}{Le} \frac{\partial}{\partial t} \Sigma(y, t) = \frac{\partial^2}{\partial y^2} \left\{ B(y) + G[\alpha(y), \Sigma(y, t)] \right\}, \quad (17)$$

with  $G(\alpha, \Sigma) = k^2 \Sigma + C^2 (\alpha - \Sigma)^2 \Sigma$ .

The stationary solutions of this equation are given by

$$\chi[y, \alpha(y), \Sigma(y)] = B(y) + G[\alpha(y), \Sigma(y)] = 0. \quad (18)$$

Regarding this as an equation for  $\Sigma$ , the number of possible solutions depends on the latitude  $y$  through the values of  $B(y)$  and  $\alpha(y)$ . We denote as  $A_+(\alpha)$  and  $A_-(\alpha)$  the maximum and the minimum of the function  $G(\Sigma)$  for  $\alpha$  and  $k$  fixed (see figure 5a). In the range of latitudes  $y$  where the value of  $(-B)$  is bounded by  $A_+$  and  $A_-$ , three solutions are obtained, since  $G$  is a *cubic* polynomial of  $\Sigma$ . When the value of  $(-B)$  is outside the interval  $[A_-, A_+]$ , there is only one solution.

In particular, since  $k \neq 0$ , the minimum  $A_-(\alpha)$  differs from zero and there exists only one equilibrium in the vicinity of  $\alpha = 0$ , which corresponds to  $y$ -latitudes close

to the equator (since the forcing is symmetric) or close to the poles (since no-flux temperature is imposed there). The asymptotic expansion is thus unable to describe multiple equilibria globally defined in the domain. Nevertheless, we will show that the asymptotic theory is a useful tool to help understand many features of the dynamic behaviour of the thermohaline model.

### 3.4. Pseudo-stability considerations

The asymptotic equation can also be expressed as

$$\frac{k}{Le} \frac{\partial}{\partial t} \Sigma(y, t) = \frac{\partial^2}{\partial y^2} \frac{\partial}{\partial \Sigma} V[y, \Sigma(y, t)] , \quad (19)$$

where  $V$  can be easily derived by a polynomial integration, such that  $\partial V[y, \Sigma] / \partial \Sigma = B(y) + G[\alpha(y), \Sigma]$ . A Lyapounov functional  $\mathcal{L}$  is given by  $\mathcal{L}\{\Sigma\} = \int_{-\pi/k}^{\pi/k} V[s, \Sigma(s, t)] ds$ . Indeed

$$\begin{aligned} \frac{d\mathcal{L}}{dt} &= \int_{-\pi/k}^{\pi/k} \frac{\partial V}{\partial \Sigma} \frac{\partial \Sigma}{\partial t} ds = \frac{Le}{k} \int_{-\pi/k}^{\pi/k} \frac{\partial V}{\partial \Sigma} \frac{\partial^3 V}{\partial^2 y \partial \Sigma} ds \\ &= -\frac{Le}{k} \int_{-\pi/k}^{\pi/k} \left[ \frac{\partial^2 V}{\partial y \partial \Sigma} \right]^2 ds \leq 0 . \end{aligned} \quad (20)$$

The last equality comes from the lateral boundary conditions on the salinity field ( $\Sigma = 0$ ) and on the function  $B$  ( $B = 0$ ), which ensure that  $\partial V / \partial \Sigma = B + G$  vanishes at  $y = \pm\pi/k$ . Since  $\mathcal{L}$  is bounded from below and monotonically decreasing in time, a steady state is reached when  $\mathcal{L}$  is a local minimum.

For a fixed  $y$ , the steady solutions of the asymptotic equation are the extrema of the potential  $V$ . If a global solution is such that the potential  $V$  is a minimum for each  $y$ , the Lyapounov functional is minimal too and the solution is thus linearly stable in the whole domain.

For a given  $y$ , multiple equilibria may exist. As  $y$  varies, at most one solution is globally defined and the others are only defined in some subinterval of the domain. A branch of solution will be called ‘stable’ when it corresponds to the absolute minimum of  $V$  and ‘metastable’ when it corresponds to a simple minimum of  $V$ . The solution corresponding to the maximum of  $V$  is unstable. The ‘stability’ feature of a solution can change following the latitude  $y$ . The terms ‘stable’ and ‘metastable’ have been chosen by analogy with the systems really deriving from a potential  $\partial \Sigma / \partial t = dV(\Sigma) / d\Sigma$ . For these systems, such as the liquid/vapour transition model, the terms stable and metastable have a well-defined meaning. For the present study, these terms are not rigorously applicable. We will thus talk about ‘pseudo-stability’ features.

Owing to the *cubic* form of the function  $G$ , the mid-value  $A_0 = (A_+ + A_-) / 2$  characterizes the location where the two minima of  $V$  have the same value. At this latitude, the pseudo-stability features of two solutions are exchanged: the ‘stable’ solution becomes ‘metastable’, while the ‘metastable’ solution becomes ‘stable’. A steady solution could be obtained through a switch from the initial ‘stable’ branch of solution to the new one. However, there is no guarantee that the resulting front is stable and can be observed numerically.

The asymptotic equation presented here is not able to describe such fronts. Attempts to bypass this difficulty have been made through regularization of this equation, either by adding a fourth-order hyperdiffusion term  $-\gamma^2 \partial^2 \Sigma / \partial y^2$  inside the braces in

equation (17), as proposed by Cessi & Young (1992), or by including the true higher-order terms in the asymptotic equation. Whatever the added terms, the study of front positioning is here not as straightforward as in the canonical case  $\partial\Sigma/\partial t = dV(\Sigma)/d\Sigma$ , because of the variation of the local potential with space through  $\alpha$ , and of the presence of the  $\partial^2/\partial y^2$  operator.

Section 4 gives a method to deduce the domain of existence of the asymptotic solutions, and the locations of the pseudo-stability exchanges.

#### 4. Geometric resolution of the asymptotic equation

We present a geometric construction which indicates, for any surface forcing, the structure of the asymptotic solutions and the possible positions of the fronts, in the vicinity of which the asymptotic expansion is not valid. In this section and the next ones, we use the notation  $\mathcal{Y} = ky$  for the latitude, with  $\mathcal{Y} \in [-\pi, \pi]$ . Because of the chosen units, the poles correspond to  $\mathcal{Y} = -\pi$  and  $\mathcal{Y} = \pi$ , while a more conventional definition of the latitude would have them at  $-\pi/2$  and  $\pi/2$ .

##### 4.1. The geometric construction

For  $\alpha$  and  $k$  fixed, the expressions for the maximum  $A_+(\alpha)$  and minimum  $A_-(\alpha)$  of  $G(\Sigma)$  are given by

$$A_{\pm}(\alpha) = \frac{2\alpha k^2}{3} + \frac{2C^2\alpha^3}{27} \pm \frac{2C^2\alpha^3}{27} \left(1 - \frac{3k^2}{C^2\alpha^2}\right)^{3/2}. \quad (21)$$

In figure 5(b), the curves  $A_+(\alpha)$  and  $A_-(\alpha)$  are displayed as thin solid lines, for an aspect ratio  $k = 0.2$ . Their mid-value  $A_0$  is plotted as a thin dashed line. For general  $k$ , the curves  $A_+(\alpha)$  and  $A_-(\alpha)$  intersect for the value  $\alpha_* = \sqrt{3} k/C$ , where  $A_+(\alpha_*) = A_-(\alpha_*) = (8/9) k^2\alpha_*$ . When  $\alpha \rightarrow \infty$ ,  $A_-(\alpha)$  is asymptotic to  $k^2\alpha$ . When  $k \rightarrow 0$ , the intersection point of  $A_+(\alpha)$  and  $A_-(\alpha)$  gets close to the origin and  $A_-(\alpha)$  tends to merge with the horizontal axis.

In order to have a global picture of the equilibria obtained by solving the equation  $G(\alpha, \Sigma) = -B(y)$ , it is convenient to plot  $[\alpha(y), -B(y)]$  as a parametric curve. We denote by  $\mathcal{B}$  the location of all the points  $[\alpha(y), -B(y)]$  reached when  $\mathcal{Y} = ky$  varies from  $-\pi$  to  $\pi$ . Since the forcing has been chosen equatorially symmetric, we just have to study the restriction of  $\mathcal{B}$  to the points such that  $\mathcal{Y} \in [-\pi, 0]$ . For example, the curve  $\mathcal{B}$  representative of the *loop* forcing in this hemisphere is displayed in figure 5(b).

When the points of the curve  $\mathcal{B}$  are located inside the domain delimited by the curves  $A_+$  and  $A_-$ , three equilibria exist for the corresponding latitudes  $\mathcal{Y}$ . Points of  $\mathcal{B}$  outside this domain correspond to latitudes where only one equilibrium is defined, following the asymptotic theory. The intersections of  $\mathcal{B}$  and  $A_0(\alpha)$  correspond to the latitudes  $\mathcal{Y}$  where the stable solution and the metastable solution exchange their pseudo-stabilities.

Examples of the geometric construction are given hereafter for the three kinds of forcing we study here. The topology of the asymptotic solutions is, in each case, deduced and explained.

##### 4.2. The loop shape forcing (FT1 and FS2)

We consider the forcing functions  $F_T(ky) = \cos(ky)$  and  $F_S(ky) = [\cos(ky) + \cos(2ky)]/2$ . The  $\alpha$ -axis is connected to the latitude axis by the relation  $\alpha = -a \sin(\mathcal{Y})$ .

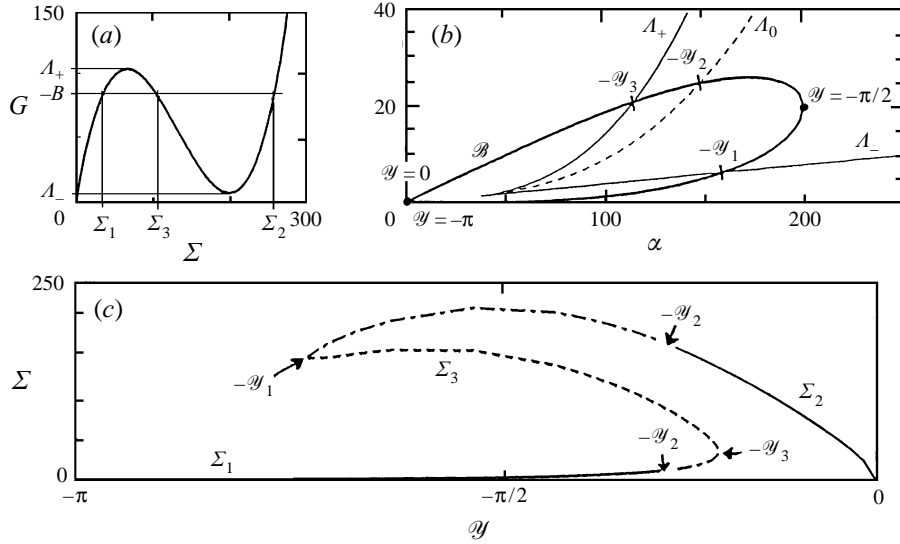


FIGURE 5. *Loop case* (FT1 and FS2): (a) Function  $G(\Sigma)$  when  $k = 0.2$  and  $\alpha = 200$ .  $A_+$  and  $A_-$  are the extrema of  $G(\Sigma)$ .  $-B$  is between  $A_+$  and  $A_-$  and the asymptotic equation has three solutions  $\Sigma_1$ ,  $\Sigma_2$  and  $\Sigma_3$ . (b) Geometrical construction. The parameters are  $a = 200$ ,  $b = 40$  and  $k = 0.2$ .  $A_+(\alpha)$  and  $A_-(\alpha)$  are displayed as thin solid lines,  $A_0(\alpha)$  as a thin dashed line. The parametric curve  $\mathcal{B}$  representative of the applied surface forcing is displayed as a solid bold line. The characteristic latitudes are denoted by  $-\mathcal{Y}_1$ ,  $-\mathcal{Y}_2$  and  $-\mathcal{Y}_3$ . (c) Solutions  $\Sigma(\mathcal{Y})$  of the asymptotic equation: stable (—), metastable (---) and unstable (· · · ·) branches of solution.

The point  $\alpha = a$  corresponds to the mid-hemisphere latitude ( $\mathcal{Y} = -\pi/2$ ) and the point  $\alpha = 0$  corresponds to the latitudes of the pole ( $\mathcal{Y} = -\pi$ ) and of the equator ( $\mathcal{Y} = 0$ ). The relation between  $B$  and  $\alpha$  is  $-B = \alpha (b_1 - b_2[1 - (\alpha^2/a^2)]^{1/2})/a$  if  $\mathcal{Y} \in [-\pi, -\pi/2]$  and  $-B = \alpha (b_1 + b_2[1 - (\alpha^2/a^2)]^{1/2})/a$  if  $\mathcal{Y} \in [-\pi/2, 0]$ . The complete curve  $\mathcal{B}$  describes a *loop* in the plane  $(\alpha, -B)$ . The *loop* is swept across following the direct trigonometric sense, when  $\mathcal{Y}$  varies from  $-\pi$  to 0.

In figure 5(b), the representation plane is  $(\alpha, -B)$ . The curves  $A_+(\alpha)$ ,  $A_-(\alpha)$ ,  $A_0(\alpha)$  and  $\mathcal{B}$  are displayed in the particular case ( $a = 200$ ,  $b = 40$ ,  $k = 0.2$ ). The notation corresponding to the intersections between  $\mathcal{B}$  and the different  $A$  curves is indicated in figure 5(b). Figure 5(c) shows the solutions  $\Sigma(\mathcal{Y})$  of the asymptotic equation, using different lines to distinguish the pseudo-stability features. Performing a reflection of figure 5(b) with respect to the equator ( $\mathcal{Y} = \phi$ ), one obtains the solutions in the second hemisphere  $[0, \pi]$ .

From  $\mathcal{Y} = -\pi$  to  $\mathcal{Y} = -\mathcal{Y}_1$ , the latitude of the intersection of  $\mathcal{B}$  and  $A_-$ , only one equilibrium  $\Sigma_1$  exists. When  $\mathcal{B}$  crosses the curve  $A_-$  at  $\mathcal{Y} = -\mathcal{Y}_1$ , two other equilibria appear. One of these solutions,  $\Sigma_2$ , is metastable (local minimum of the potential  $V$ , defined in § 3.4) and the other,  $\Sigma_3$ , is unstable (maximum of the potential  $V$ ). When  $\mathcal{B}$  crosses the curve  $A_0$  at  $\mathcal{Y} = -\mathcal{Y}_2$ , the pseudo-stabilities of two equilibria are exchanged: the metastable solution  $\Sigma_2$  becomes stable, while the initial solution  $\Sigma_1$  becomes metastable. The third solution remains unstable. When  $\mathcal{B}_2$  intersects  $A_+$  at  $\mathcal{Y} = -\mathcal{Y}_3$ , the two solutions  $\Sigma_1$  and  $\Sigma_3$  disappear. The only remaining solution  $\Sigma_2$  is the stable one.

Because of the relation  $\Psi = [\Sigma - \alpha] P(z)$ , one could superpose  $\alpha = -a \sin(\mathcal{Y})$  on the  $\Sigma$  graph of figure 5(c) to determine the sign of the streamfunction  $\Psi$  for

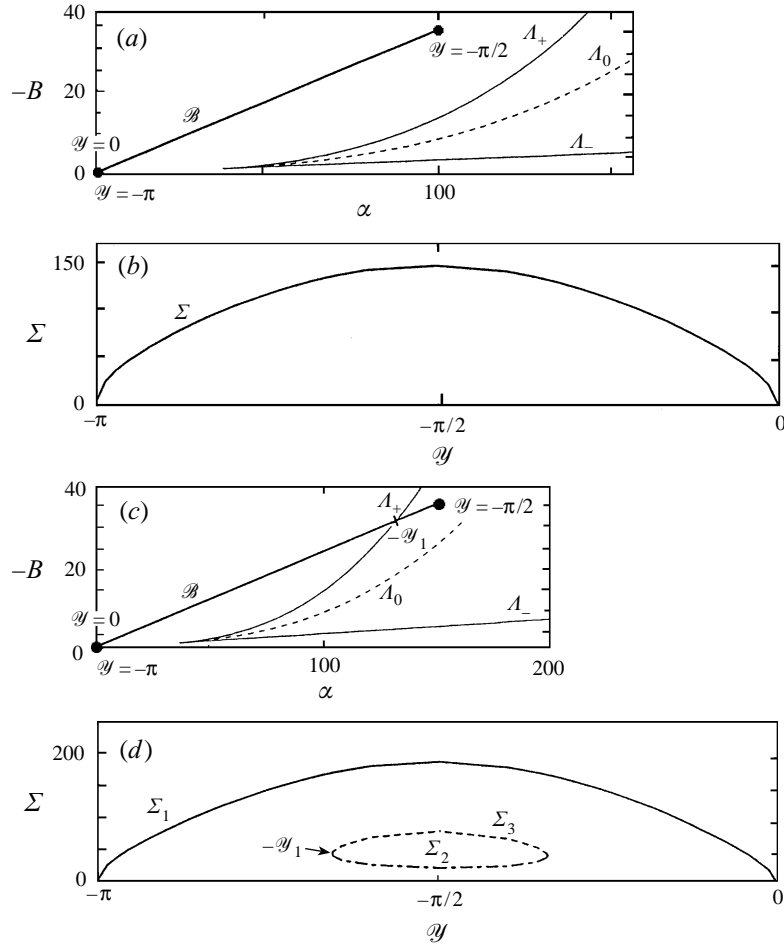


FIGURE 6 (a-d). For caption see facing page.

each equilibrium. Since the meridional salinity gradient  $\Sigma_1$  is much weaker than  $\alpha$ , the corresponding streamfunction  $\Psi_1$  corresponds to an intense thermally driven circulation.  $\Sigma_2$  induces a weak salinity-driven circulation  $\Psi_2$ . Following the asymptotic theory, a front should appear between the two counter-rotating circulations in the region where both  $\Sigma_1$  and  $\Sigma_2$  exist. It must be located in the interval  $[-y_1, -y_3]$ , but not necessarily at  $y = -y_2$  since the concept of metastability is not rigorously defined for the asymptotic equation.

A detailed comparison of analytical predictions and numerical results with these forcing and parameters is given in §5 and shows that the asymptotic analysis is pertinent for an aspect ratio as large as  $k = 0.2$ .

#### 4.3. The straight line shape forcing (FT1 and FS1)

The forcing functions  $F_T(ky) = \cos(ky)$  and  $F_S(ky) = \cos(ky)$  are now applied. The relation between  $B$  and  $\alpha$  is linear (*straight*):  $-B = (b/a)\alpha$  (see figure 6). Both the functions  $B$  and  $\alpha$  are symmetric with respect to  $y = -\pi/2$  and the segment  $\mathcal{B}$  is swept across twice for a hemisphere. With this forcing, the plane  $(\alpha, -B)$  is identical to the plane  $(a, b)$ .

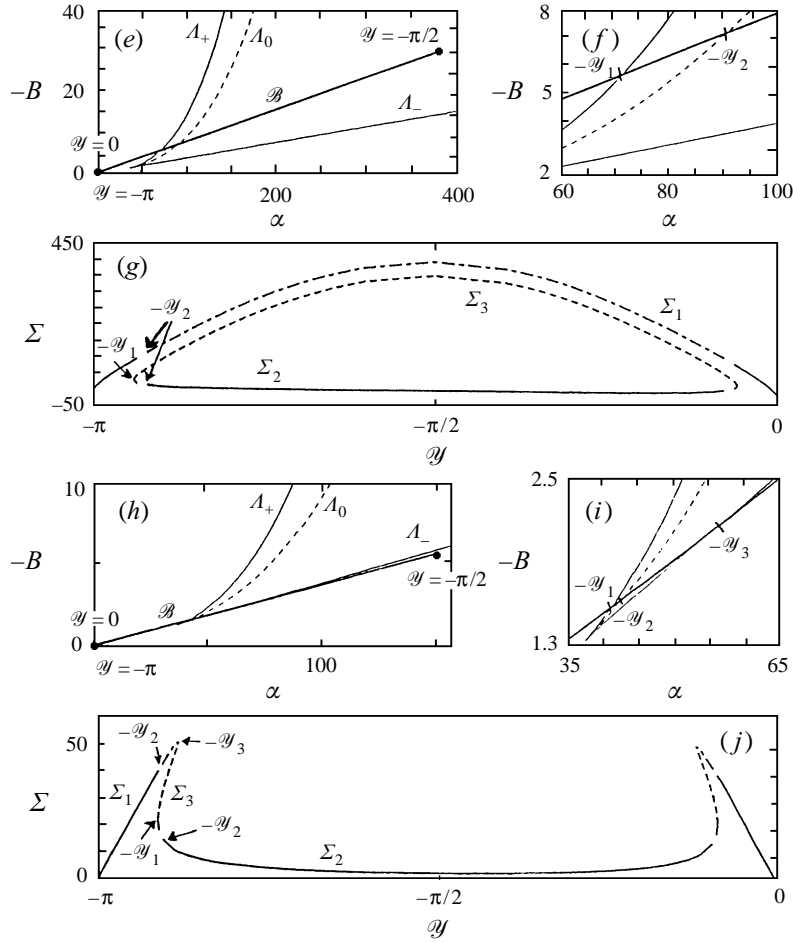


FIGURE 6. *Straight case* (FT1 and FS1): geometrical construction and solution(s)  $\Sigma(\psi)$  of the asymptotic equation. Same lines are used as in figure 5. Four sets of parameters are shown: (a, b)  $a = 100$ ,  $b = 35$  and  $k = 0.2$ . (c, d)  $a = 150$ ,  $b = 35$  and  $k = 0.2$ . (e-g)  $a = 380$ ,  $b = 30$  and  $k = 0.2$ . (h-j)  $a = 150$ ,  $b = 5.75$  and  $k = 0.2$ .

As detailed by Thual & McWilliams (1992), a ‘zero-circulation line’ exists in this case (and for  $Le = 1$ ), which separates the domain of existence of salinity-driven circulations and thermally driven circulations in the plane  $[a, b]$ . For magnitudes of the forcing located on this line, the thermal and saline effects exactly balance in the two-dimensional Boussinesq model, and the circulation vanishes in the whole box. The ‘zero-circulation line’ equation reads  $b = ak \tanh(k)$ . In the limit of a small aspect ratio  $k$  it merges with the asymptote of  $A_-$ , the slope of which is  $k^2$  in the plane  $(\alpha, -B)$ . The branch of solution initiated at  $\psi = -\pi$  is a temperature-driven one if the segment  $\mathcal{B}$  is below the ‘zero-circulation line’. It is a salinity-driven circulation otherwise.

We can distinguish different topological behaviours depending on the number of intersections of  $\mathcal{B}$  with the different  $A$  curves:

(i) If there is no intersection of  $\mathcal{B}$  with any  $A$  curve (figure 6a), there is only one solution in the whole basin. Figures 6(a) and 6(b) present the geometric construction

and the asymptotic solution  $\Sigma(\mathcal{Y})$  in such a case, with the parameters ( $a = 100$ ,  $b = 35$ ,  $k = 0.2$ ).

(ii) If  $\mathcal{B}$  crosses only  $A_+$  (figure 6c), only one solution exists between the latitude  $\mathcal{Y} = -\pi$  and the intersection of  $\mathcal{B}$  and  $A_+$  at  $\mathcal{Y} = -\mathcal{Y}_1$ . There, two new solutions appear. They exist on an interval symmetric with respect to  $\mathcal{Y} = -\pi/2$ . One of them,  $\Sigma_2$ , is metastable on its definition domain, the other one,  $\Sigma_3$ , is unstable. The globally defined solution  $\Sigma_1$  is stable on the whole box. Figure 6(c) and 6(d) show the situation with the parameters ( $a = 150$ ,  $b = 35$ ,  $k = 0.2$ ).

(iii) If  $\mathcal{B}$  crosses successively  $A_+$  and  $A_0$  (figures 6e and 6f), the metastable solution  $\Sigma_2$ , which appears at  $\mathcal{Y} = -\mathcal{Y}_1$  when  $\mathcal{B}$  cuts  $A_+$ , becomes stable when  $\mathcal{B}$  cuts  $A_0$  at  $\mathcal{Y} = -\mathcal{Y}_2$  and remains stable from  $\mathcal{Y} = -\mathcal{Y}_2$  to the mid-hemisphere. The initial solution  $\Sigma_1$  is metastable between  $-\mathcal{Y}_2$  and the mid-hemisphere. The solutions are symmetric with respect to the half-hemisphere. In the whole hemisphere, two fronts can exist: at the locations  $-\mathcal{Y}_2$  and  $\mathcal{Y}_2 - \pi$ , the solution could switch from  $\Sigma_1$  to  $\Sigma_2$  or could stay on the metastable solution  $\Sigma_1$ . Such a behaviour is displayed for the parameters ( $a = 380$ ,  $b = 30$ ,  $k = 0.2$ ) in figures 6(e), 6(f) and 6(g). Some comparisons performed in this case between numerical results and analytical predictions are presented in §6.

(iv) The fourth case happens when  $\mathcal{B}$  crosses successively  $A_+$ ,  $A_0$  and  $A_-$  (figures 6h and 6i). This is possible, only if the slope of  $\mathcal{B}$  is between  $8k^2/9$  and  $k^2$ . All the branches of solutions are thus thermally driven. Before  $\mathcal{B}$  cuts  $A_+$ , there is only one solution  $\Sigma_1$ . When  $\mathcal{B}$  cuts  $A_+$  at  $\mathcal{Y} = -\mathcal{Y}_1$ , two new solutions appear, one of them,  $\Sigma_2$ , is metastable, the other one,  $\Sigma_3$ , unstable. When  $\mathcal{B}$  cuts  $A_0$  at  $\mathcal{Y} = -\mathcal{Y}_2$ , the metastable solution becomes stable and inversely. When  $\mathcal{B}$  cuts  $A_-$  at  $\mathcal{Y} = -\mathcal{Y}_3$ , the metastable  $\Sigma_1$  and unstable  $\Sigma_3$  solutions merge and vanish. The scheme is symmetric with respect to the half-hemisphere. Figures 6(h), 6(i) and 6(j) show an example with the parameters ( $a = 150$ ,  $b = 5.75$ ,  $k = 0.2$ ).

When  $k \rightarrow 0$ ,  $A_-$  tends to merge with the horizontal axis  $b = 0$ ,  $A_+$  becomes a *cubic* curve of  $\alpha$ , and the intersection point between  $A_-$  and  $A_+$  moves to the origin, as found by Thual & McWilliams (1992) from their numerical experiments. In this limit, multiple equilibria are globally defined in the domain provided the line representative of the forcing is entirely included in the domain delimited by  $A_-$  and  $A_+$ .

#### 4.4. The cubic shape forcing (FT2 and FS1)

Here, the forcing functions are  $F_T(ky) = -2 \int_{-\pi/k}^y k \sin^{1/3}(ks) ds / \int_{-\pi/k}^0 k \sin^{1/3}(ks) ds$  and  $F_S(ky) = \cos(ky)$ . The relation between  $\alpha$  and the latitude  $\mathcal{Y} = ky$  is more complicated than in the previous cases since  $\alpha = -2 \sin^{1/3}(\mathcal{Y}) / \int_{-\pi}^0 \sin^{1/3}(Y) dY$ . The parametric curve representative of the surface forcing (figure 7b) is expressed with the *cubic* form  $-B \propto -(b/a^3) \alpha^3$ , which explains the choice of the complex expression for FT2. It is swept across twice for a hemisphere.

Figure 7(a) compares the temperature forcing profiles  $T(y, 0) = 488 \times \text{FT2}(ky)$  and  $T(y, 0) = 380 \times \text{FT1}(ky)$  of, respectively, the *cubic* and *straight* cases, which share, otherwise, the same FS1 salinity forcing. The relation between the magnitudes (488 and 380) of the thermal forcings has been chosen such that the two profiles have the same slope at  $\mathcal{Y} = \pm\pi/2$ . They are obviously very close to each other, except around the poles and the equator. The differences between the two forcings at these latitudes generate significant differences in the corresponding asymptotic solutions.

The geometric constructions for the two surface forcings [ $380 \times \text{FT1}(ky)$ ,  $40 \times \text{FS1}(ky)$ ] and [ $488 \times \text{FT2}(ky)$ ,  $40 \times \text{FS1}(ky)$ ] are portrayed in figure 7(b), for an aspect

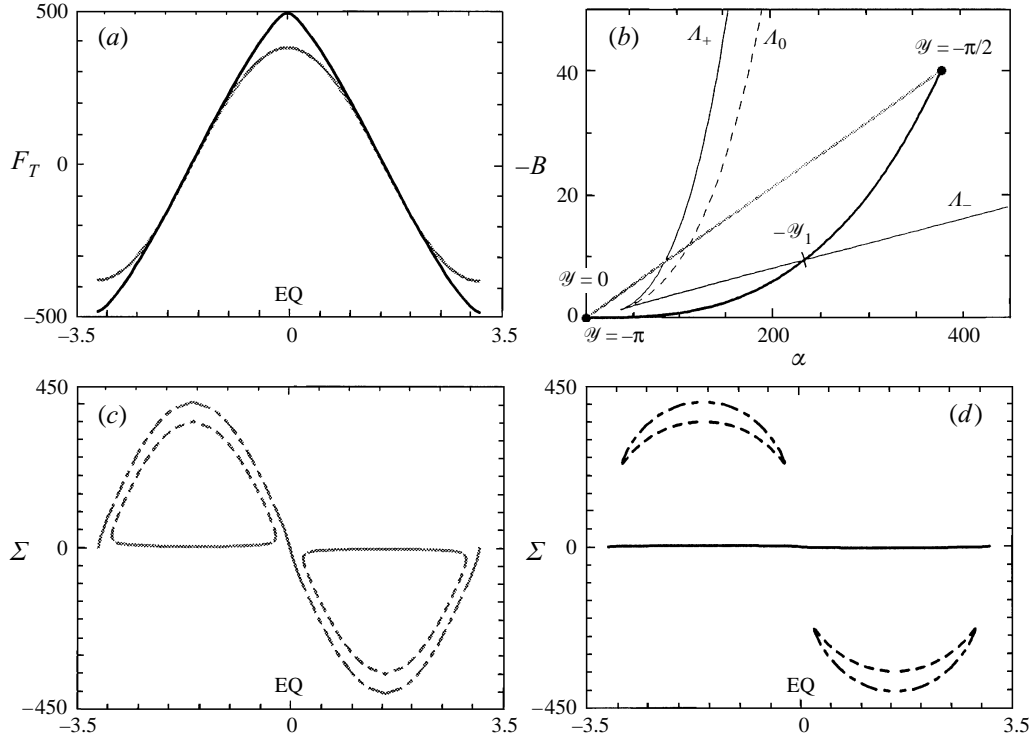


FIGURE 7. (a) Surface temperature forcing  $380 \times \text{FT1}$  (grey) (*straight* case) and  $488 \times \text{FT2}$  (dark) (*cubic* case). (b) Geometrical construction with the forcing and parameters  $k = 0.2$ ,  $40 \times \text{FS1}$ ,  $380 \times \text{FT1}$  (*straight* case, grey) and  $k = 0.2$ ,  $40 \times \text{FS1}$ ,  $488 \times \text{FT2}$  (*cubic* case, dark). (c) Asymptotic solutions  $\Sigma(\mathcal{Y})$  in the *straight* case. (d) Asymptotic solutions  $\Sigma(\mathcal{Y})$  in the *cubic* case. Same lines are used as in figure 5.

ratio  $k = 0.2$  and the whole domain  $\mathcal{Y} \in [-\pi, \pi]$ . While the surface forcings are similar, the two curves  $\mathcal{B}$  are very different. In the *straight* case (FT1),  $\mathcal{B}$  crosses successively  $A_+$  and  $A_0$  (see case iii, §4.3) while, applying the *cubic* forcing (FT2),  $\mathcal{B}$  crosses only  $A_-$ . In this last case, the initial branch of solution remains stable on the whole basin, while the two equilibria appearing when  $\mathcal{B}$  crosses  $A_-$  at  $\mathcal{Y} = -\mathcal{Y}_1$  stay respectively metastable and unstable on their definition domain, which is symmetrical about the mid-hemisphere.

The associated solutions are displayed in figure 7(c) (*straight* case) and figure 7(d) (*cubic* case). In the *straight* case, the globally defined solution is the salinity-driven one (characterized by higher values of  $\Sigma$ , the meridional gradient of the depth-averaged salinity), while in the *cubic* case, it is the thermally driven one. This discussion is continued in §7.3, where the numerical solutions associated to the two sets of surface forcing are compared.

Considering the stability of the solutions obtained in the *cubic* case, one could think that the globally defined solution is the only one that might be observed. But we recall here that the terms ‘stable’ and ‘metastable’ have just been chosen to distinguish the absolute minimum of the potential from its local minimum. Here, the criterion to determine whether a locally defined solution can be observed or not is also linked to the width of its definition domain, as will be discussed in §6.2. In the example

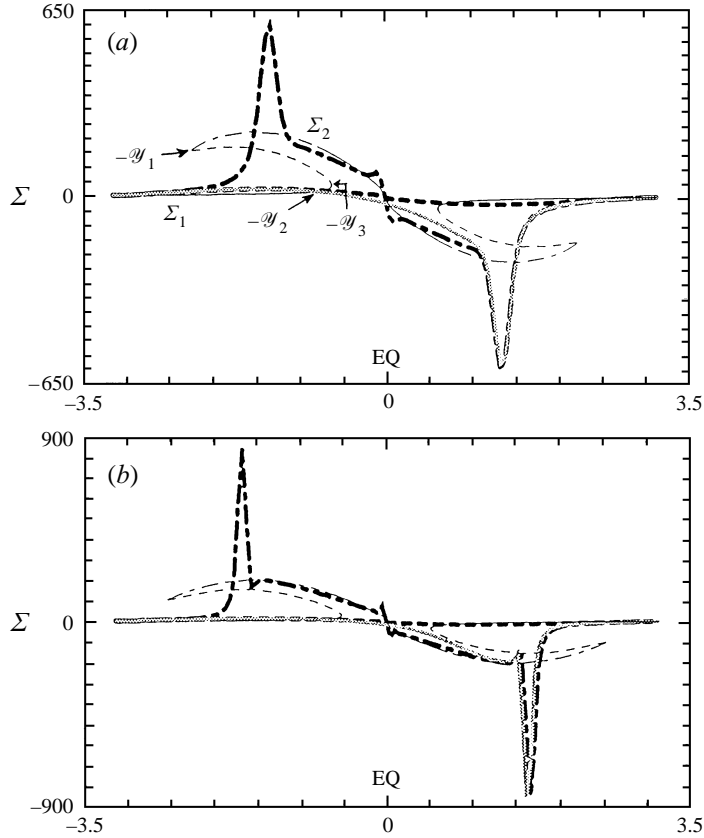


FIGURE 8.  $\Sigma(y)$  in the *loop* case (FT1 and FS2). Theoretical solutions are thin lines: stable (—), metastable (---) and unstable (- - -) branches of solution. Numerical solutions are bold lines: TH (---), 4C (---) and A2C (grey solid line). (a)  $a = 200$ ,  $b = 40$  and  $k = 0.2$ . (b)  $a = 180$ ,  $b = 20$  and  $k = 0.1$ .

displayed in figure 7(d), the metastable solution exists on a ‘large’ part of the box and is certainly observable.

## 5. Numerical simulations for the *loop* case (FT1 and FS2)

We recall that the numerical results obtained in this case are presented in figure 2 and the geometrical construction is explained in figure 5. Figure 8, 9 and 10 show some comparisons between numerical and asymptotic results, which are detailed below.

### 5.1. Structure of the solutions

Figure 2 presents the equilibria obtained with the forcing profiles FT1 and FS2 and the parameters ( $a = 200$ ,  $b = 40$ ,  $k = 0.2$ ). For each equilibrium, the temperature and salinity fields have a similar vertical structure, which is almost homogeneous, as predicted by the asymptotic analysis.

The observed equilibria can be analysed by comparison with the asymptotic solutions. In figure 8(a) the solutions of the asymptotic equation are displayed on the whole domain  $y \in [-\pi, \pi]$  as thin lines; bold lines have been chosen to represent the latitudinal gradients  $\Sigma_{num}$  of the depth-averaged salinity, calculated for the numerical

equilibria in figure 2. In figure 8(b), similar curves are obtained for the parameter set ( $a = 180$ ,  $b = 20$ ,  $k = 0.1$ ). We use the notation  $-\mathcal{Y}_1$ ,  $-\mathcal{Y}_2$ ,  $-\mathcal{Y}_3$  for the characteristic latitudes and  $\Sigma_1$ ,  $\Sigma_2$ ,  $\Sigma_3$  for the theoretical solutions, as defined in figure 5(c).

The observed stationary fronts (figures 2b and 2c) correspond to discontinuities of the salinity field; their signatures are approximatively Dirac functions of the salinity gradient  $\Sigma_{num}$  (figure 8). In the vicinity of the fronts, boundary layers develop; they are visible in figures 8(a) and 8(b). The width of the boundary layers obviously decreases when  $k$  is decreased; the fronts at mid-hemispheres go to Dirac functions of the variable  $\Sigma_{num}$ . In the boundary layers, the slow  $y$ -dependence hypothesis is not relevant anymore, and the asymptotic expansion is not valid.

In the case of the thermally driven circulation (TH, figure 2a),  $\Sigma_{num}$  (figure 8, bold dashed line) stays very close to the stable solution  $\Sigma_1$  between the pole and the latitude  $-\mathcal{Y}_2$ , and symmetrically with respect to the equator. On the interval  $[-\mathcal{Y}_2, \mathcal{Y}_2]$ , a boundary layer develops and connects the two branches of  $\Sigma_1$ . The asymptotic analysis is not valid in such a boundary layer.

Fronts connecting the  $\Sigma_1$  and  $\Sigma_2$  solutions appear in the equilibrium exhibiting four cells of circulation (4C, figure 2b). The topology of this equilibrium thus follows the scheme predicted by the asymptotic analysis. Near the poles, the solution  $\Sigma_{num}$  (figure 8, bold dot-dashed line) is close to the single asymptotic solution  $\Sigma_1$  and, in both hemispheres, jumps through a front to the asymptotic solution  $\Sigma_2$  which is defined and stable close to the equator.

The slighter discontinuity observed at the equator ( $\mathcal{Y} = 0$ ) is not predicted by the asymptotic equation. It corresponds to a pinching of the streamlines (figure 2b). The narrowing of downwelling regions in the ocean has been addressed by Stommel (1962) at high values of the forcing. Here, the pinching phenomenon occurs at low values of the forcing.

The asymmetric circulations (A2C, figure 2c and its reflection with respect to the equator) are composed according to the ‘superposition principle’ (see §2.4). Indeed,  $\Sigma_{num}$  (figure 8, grey solid line) merges with the  $\Sigma_{num}$  branch of the TH solution on the most important part of one hemisphere and with the  $\Sigma_{num}$  branch of the four-celled solution on a large part of the other hemisphere. A large boundary layer develops and connects the two solutions across the equator.

Comparing results obtained with  $k = 0.2$  (figure 8a) and  $k = 0.1$  (figure 8b), we observe that the agreement between  $\Sigma_{num}$  and the asymptotic prediction improves when the aspect ratio is decreased.

## 5.2. Further validation of the asymptotic equations

We compare the locations of the numerically observed fronts to the locations predicted by the geometric construction. For the equilibria presented in figure 2, the numerical mid-latitude fronts are located at  $\mathcal{Y} = -0.44\pi$  in the first hemisphere, while the characteristic intersections of the geometric construction are  $-\mathcal{Y}_1 = -0.70\pi$ ,  $-\mathcal{Y}_2 = -0.27\pi$  and  $-\mathcal{Y}_3 = -0.18\pi$ . The numerical location of the fronts is thus between  $-\mathcal{Y}_1$  and  $-\mathcal{Y}_2$ . This result has been observed in all our simulations; the position of the fronts exhibits a maximal departure of 20% from the mid-value  $-(\mathcal{Y}_1 + \mathcal{Y}_2)/2$ . If the asymptotic equation does not predict accurately the frontal location, the observed fronts are always located in the domain of existence of multiple asymptotic solutions. The poor agreement between the numerical and the predicted positions of the fronts could be attributed to the relatively large aspect ratio used in numerical simulations, or the fact that the metastability concept is not rigorously defined in this problem.

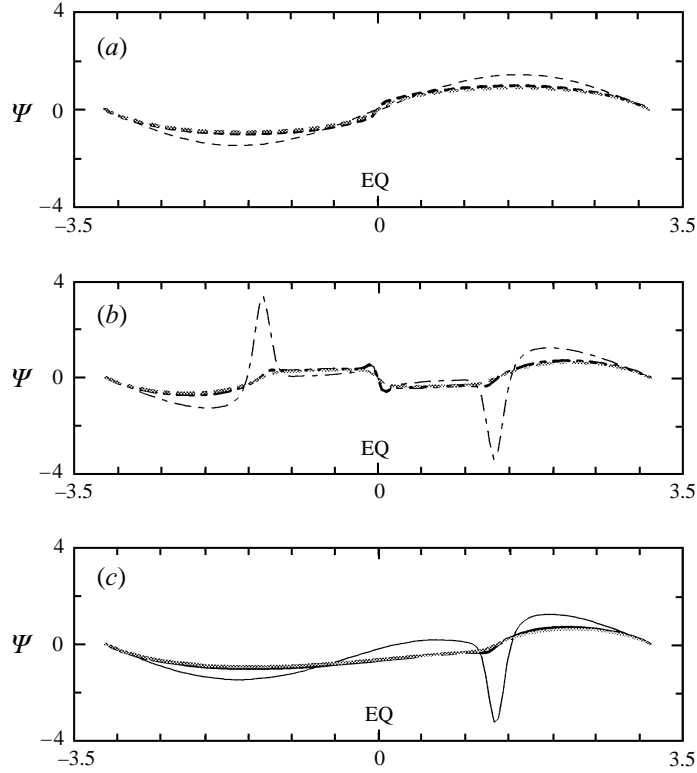


FIGURE 9. Depth-averaged streamfunctions for the *loop* forcing (FT1 and FS2) and the parameters  $a = 200$ ,  $b = 40$  and  $k = 0.2$ . Grey lines:  $\bar{\Psi}_{num}$ . Dark bold lines:  $\bar{\Psi}_1(\Sigma_{num}, \Theta_{num})$ . Dark thin lines:  $\bar{\Psi}_1(\Sigma_{num}, \alpha)$ . (a) TH solution. (b) 4C solution. (c) A2C solution.

Different diagnostics applied to the numerical results are now detailed in order to validate the asymptotic equations.

First, the latitudinal gradient of the depth-averaged numerically computed temperature  $\Theta_{num}$  is compared to the equivalent asymptotic field at the first order, which is  $\alpha$ . For the three equilibria displayed in figure 2,  $\Theta_{num}$  (not shown) exhibits values almost half those of  $\alpha$  in the range of latitudes far from the fronts. Thus, the asymptotic equality between the gradient of temperature at the first order and its forcing is not fulfilled by the numerical results. The asymptotic prediction for temperature at the second order does not give better results.

In figures 9(a), 9(b) and 9(c),  $\bar{\Psi}_{num}$ , the depth-averaged numerical streamfunction is drawn as grey lines for each of the equilibria displayed in figure 2. It is compared to the depth-averaged asymptotic streamfunction at the first order (see equation (16)), calculated by two methods. For the bold curves, the numerical temperature gradient  $\Theta_{num}$  is used [ $\bar{\Psi}_1(\Sigma_{num}, \Theta_{num}) = (\Sigma_{num} - \Theta_{num}) \int_{-1}^0 P(z) dz = \frac{1}{120} (\Sigma_{num} - \Theta_{num})$ ], while for the thin curves the asymptotically predicted value  $\alpha$  is used [ $\bar{\Psi}_1(\Sigma_{num}, \alpha) = \frac{1}{120} (\Sigma_{num} - \alpha)$ ].

Since the Prandtl number  $\sigma$  is chosen infinite,  $\bar{\Psi}_{num}$  satisfies  $\nabla^4 \bar{\Psi}_{num} = (\partial^4 \bar{\Psi}_{num} / \partial y^4 + 2\partial^4 \bar{\Psi}_{num} / \partial y^2 \partial z^2 + \partial^4 \bar{\Psi}_{num} / \partial z^4) = (\Sigma_{num} - \Theta_{num})$ , and  $\bar{\Psi}_1(\Sigma_{num}, \Theta_{num})$  results from  $\partial^4 \bar{\Psi}_1 / \partial z^4 = (\Sigma_{num} - \Theta_{num})$ . Thus, the difference between this two values corresponds only to the influence of the terms in  $\partial / \partial y$  in the bi-Laplacian of  $\Psi$ . Obviously, the two

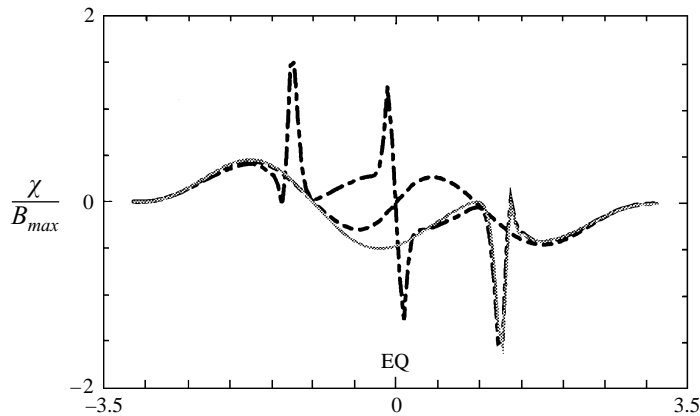


FIGURE 10. Function  $\chi[\mathcal{Y}, \Theta_{num}(y), \Sigma_{num}(y)]$  displayed following  $\mathcal{Y}$  in the *loop* case (FT1 and FS2) with  $a = 200$ ,  $b = 40$  and  $k = 0.2$ . TH solution ( - - - - ), 4C solution ( - - - - ) and A2C solution (grey solid line).

curves almost merge for the three equilibria (figure 9) and the asymptotic hypothesis of a slow  $y$ -dependence is valid for the viscosity term.

The discrepancy between  $\bar{\Psi}_1(\Sigma_{num}, \Theta_{num})$  and  $\bar{\Psi}_1(\Sigma_{num}, \alpha)$  is a measure of the departure of the numerical temperature gradient from its asymptotic prediction at the first order. The asymptotic value  $\alpha$  mainly overestimates the temperature gradient and, thus, its effect on the circulation. In  $\bar{\Psi}_1(\Sigma_{num}, \alpha)$ , the thermally driven *loops* are intensified, compared to the numerical values, while the salinity-driven loops are reduced in magnitude.

The  $\chi$ -function (defined in equation (18) §3.3) is now calculated, using  $\Sigma_{num}$  and  $\Theta_{num}$  as variables. Figure 10 presents the normalized function  $\chi(\mathcal{Y}, \Theta_{num}, \Sigma_{num})/B_{max}$  for the three equilibria displayed in figure 2, where  $B_{max}$  is the maximum value of  $B$ . The  $\chi$ -function is the right-hand member of the asymptotic equation and is required to vanish for a theoretical equilibrium. We see that, except at the fronts, the curves  $\chi(\mathcal{Y}, \Theta_{num}, \Sigma_{num})/B_{max}$  exhibit departures from zero of less than 0.5. This gives a measure of the distance between asymptotic and numerical solutions. While unpredicted by the asymptotic theory, the ‘pinching discontinuity’ (see §5.1) in the 4C solution appears as a singularity of  $\chi(\mathcal{Y}, \Theta_{num}, \Sigma_{num})$  even more important than the ones corresponding to the asymptotically predicted fronts of the solutions 4C and A2C.

To summarize this part, the asymptotic theory gives a relatively good prediction of the numerical solutions far from the fronts. In a large part of the domain, the different  $\Sigma_{num}$  can reasonably be approximated by the solutions of the asymptotic equation. But, the asymptotic theory does not determine accurately the position of the fronts and the temperature solutions, for the values of the aspect ratio  $k$  explored. Moreover, a front appears at the equator in the 4C circulation, which is not asymptotically predicted. It certainly results from the pinching effect of downwelling.

The prediction is better as  $k$  is decreased. In particular, the boundary layers around the fronts, in which the asymptotic analysis is not valid, become thinner. With our numerical analysis, it is not possible to determine whether the fronts positions tend to merge to the locations of the pseudo-stability exchanges when  $k \rightarrow 0$ . Numerical simulations with aspect ratios lower than  $k = 0.1$  would be needed but are very costly.

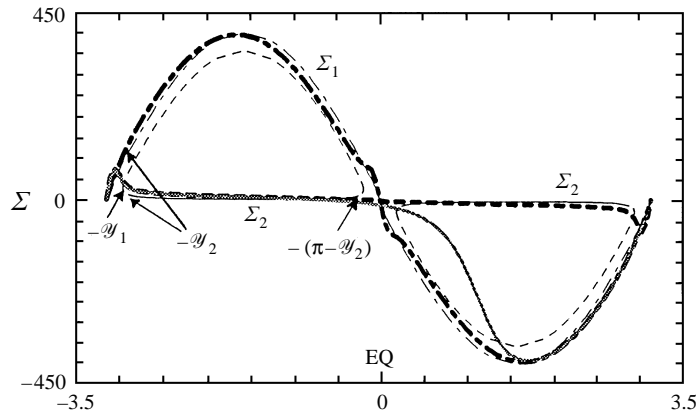


FIGURE 11.  $\Sigma(y)$  with the *straight* forcing (FT1 and FS1) and the parameters  $a = 380$ ,  $b = 30$  and  $k = 0.2$ . Theoretical solutions are thin lines: stable (—), metastable (---) and unstable (· · ·) branches of solution. Numerical solutions are bold lines: TH (---), SA (— · —) and PP (grey solid line).

## 6. Numerical simulations in the *straight* case (FT1 and FS1)

The numerical results obtained in this case are presented in figure 3. With the set of parameters used here, the topology of the solutions corresponds to the third case discussed in §4.3. The asymptotic solutions are displayed in figure 6(g). Figures 11 to 15 show some comparisons between numerical and asymptotic results, which are explained below.

### 6.1. Structure of the solutions

The equilibria obtained with the forcing functions FT1 and FS1 and the parameters ( $a = 380$ ,  $b = 30$ ,  $k = 0.2$ ) are displayed in figure 3. Numerically, multiple equilibria are observed, while only one theoretical solution is defined on the whole domain. Indeed, in the vicinity of  $\sin(y) = 0$ , boundary layers can develop and extend a locally defined asymptotic solution on the latitudinal intervals, in which it is not defined. Figure 11 presents a comparison between the solutions of the asymptotic equation (thin lines) and  $\Sigma_{num}$  (bold lines) computed from the three equilibria of figure 3. The good agreement between asymptotic predictions and numerical observations is obvious in figure 11. The notation  $-y_1$ ,  $-y_2$  for the characteristic latitudes and  $\Sigma_1$ ,  $\Sigma_2$ ,  $\Sigma_3$  for the theoretical solutions is defined in figure 6(g). We introduce now an important notation, which is  $\delta = 2(\pi - y_2)$ , the distance between the two stable branches of the  $\Sigma_2$  solution around the equator. Because of symmetry across the mid-hemisphere the distance between the pole and  $-y_2$  is also  $\delta/2$ .

The set of parameters corresponding to figure 11 is such that the *straight* line representative of the forcing in the geometric construction is above the ‘zero-circulation line’ (see §4.3 for a definition). Following the asymptotic theory, the initial solution  $\Sigma_1$  is thus a salinity-driven one. Indeed,  $\Sigma_{num}$  (figure 11, bold dot-dashed line) computed from the SA solution (figure 3b) is very close to the theoretical globally defined solution, except on a very thin belt of latitudes around the equator. This singularity can be attributed to the pinching effect of downwelling, already mentioned in §5.1.

In the vicinity of the poles, the thermally driven circulation (TH, figure 3a) exhibits a  $\Sigma_{num}$  profile (figure 11, bold dashed line) which follows the asymptotic solution  $\Sigma_1$ . When the  $\Sigma_2$  solution becomes stable, the TH circulation jumps to  $\Sigma_2$ . Polar boundary

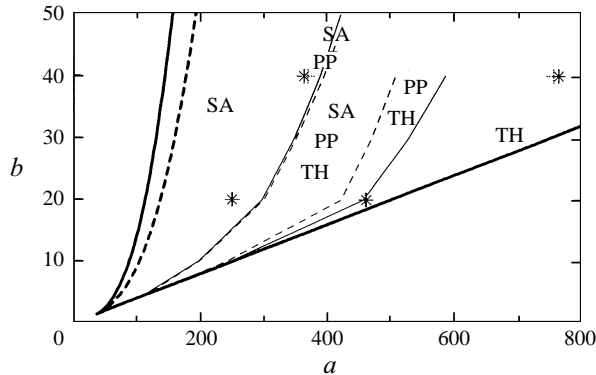


FIGURE 12. Domain of existence of multiple equilibria in the plane  $(a, b)$  with the *straight* forcing (FT1 and FS1) and  $k = 0.2$ . Bold lines: curves calculated from the asymptotic theory. Thin lines: delimiting curves computed with a low horizontal resolution (33 points). Points of delimiting curves computed with a higher resolution (129 points) are indicated by \* and +.

layers connect the solutions  $\Sigma_1$  and  $\Sigma_2$  to each other. The distance of such a polar front to the pole is of order  $\delta/2$ . When  $\delta/2$  is large enough, counter-rotating cells are observed (not shown) and are explained by our present analysis. Near the equator, a boundary layer of size  $\delta_E \sim \delta$  connects the two local branches of the  $\Sigma_2$  solution to each other. This boundary layer is visible as squeezed streamlines at the equator in figure 3(a).

The pole-to-pole equilibria (PP, figure 3c and its reflection with respect to the equator) are the combination of the TH circulation in one hemisphere and the SA circulation in about half of the other hemisphere. The  $\Sigma_{num}$  representation (figure 11, grey solid line) shows that the two branches are connected together by a large boundary layer, developing in the hemisphere with the less intense circulation. The ‘superposition principle’ (see §2.4) is respected, but the limit between the two different parts does not appear exactly at the equator.

### 6.2. Domain of existence of multiple equilibria

We have obtained a great number of numerical solutions with the forcing profiles FT1 and FS1 (*straight*) and the parameters  $k = 0.2$ ,  $Le = 1$  and  $\sigma = \infty$ . Low horizontal resolution with only 33 points for both hemispheres has been used for this exploration. The domains of existence of the different circulations TH, SA and PP are located. Figure 12 shows the five different regions that can be identified in the plane  $(a, b)$ . With the present surface forcing, this plane is equivalent to the plane  $(\alpha, -B)$ . In these domains, from the bottom up, there exists only one solution TH, two solutions TH and PP, three solutions TH, PP and SA, two solutions SA and PP and, finally, only one solution SA.

Detailed numerical experiments for the fourth case of §4.3, corresponding to figure 6(j), could exhibit multiple TH equilibria. We have not investigated this case.

The curves  $A_-$ ,  $A_0$  and  $A_+$  are displayed as bold lines in figure 12. The part of the plane supporting numerical multiple equilibria of type TH/SA/PP is located in the domain bounded by the curves  $A_0$  and  $A_-$ , but is really narrower. The lower branch of the domain is located very close to the curve  $A_-$  when  $a$  is less than 300, but moves progressively away when  $a$  increases. The upper branch of the numerical domain is far from  $A_0$ . We now use the above boundary layer analysis to explain these differences.

Multiple equilibria are only studied with forcing parameters corresponding to the third case of §4.3 and the figure 6(g). In this case, the globally defined solution is a salinity-driven one. A TH solution is observed when the two branches of  $\Sigma_2$  (see figure 11 and §6.1) are connected to each other across the equator by a boundary layer of length  $\delta_E \sim \delta$ . The numerical simulations show that the TH solution can be observed only if  $\delta$  is small enough. When  $\delta$  is greater than a critical value  $\delta_{max}$ , the boundary layers cannot join the two branches across the equator and only the SA solution is observed numerically. Using the geometric construction detailed in §4, we have estimated this critical value of  $\delta$  to be approximately equal to  $\delta_{max} = 0.15 \times 2\pi$ , i.e. 30% of one hemisphere.

Inversely, if  $\delta$  is too small, the SA solution is only stable on a very small domain close to the poles and around the equator and it will not be observed, although it is the globally defined one. In figure 12, the right-hand part of the plane supports only a TH solution, while the *straight* line representative of the surface forcing is located above the ‘zero-circulation line’. There,  $\delta/2$  is so small that the solution always jumps from the zero boundary condition to the solution  $\Sigma_2$ . This happens when the distance needed to connect the two branches of TH circulation is less than about  $\delta_{min} = 0.04 \times 2\pi$ , i.e. 8% of one hemisphere.

The criterion to observe multiple equilibria is then a combination of the pseudo-stability features of the solutions and the width of their definition domains.

To estimate the influence of the horizontal resolution, we have used a four times greater resolution (129 points for both hemispheres) and have located some points of the curves delimiting the regions of existence of numerical multiple equilibria. They are indicated by stars (delimiting regions with only one equilibrium from regions with two equilibria) and plus signs (delimiting regions with two equilibria from the region with three equilibria) in figure 12. We note that stars and plus signs are almost superposed, which indicates that the domains of two and three equilibria merge when the resolution increases. The ‘superposition principle’ is then perfectly satisfied with a high horizontal resolution. The domain supporting numerical multiple equilibria becomes wider and closer to the asymptotically predicted domain when the resolution is increased. Wider boundary layers can exist and connect two branches of the TH solution, and the SA solution can be observed even if it is stable on a range of latitudes smaller than 8% of one hemisphere.

With increased resolution, the domain of numerical multiple solutions could become larger. The differences between the domains in figure 12 suggest that  $\delta_{min}$  could be considerably reduced by increasing the resolution. But the threshold value  $\delta_{max}$  seems to be less dependent on resolution. In spite of increasing the resolution, it would not be possible to join two branches of solution across the equator with a ‘too large’ boundary layer.

### 6.3. Further validation of the asymptotic equations

The same diagnostics as the ones in §5.2 are applied here to the numerical results.

The asymptotic value of the gradient of temperature at the two first orders is compared to  $\Theta_{num}$  (not shown) for the three equilibria of figure 3. In the TH circulation,  $\Theta_{num}$  is quite constant on each hemisphere, except close to the latitudes  $\sin(\vartheta) = 0$  where there are boundary layers and fronts. The asymptotic prediction of  $\Theta_{num}$  at the first order is  $\alpha$ , which is a cosine function and does not represent correctly the profile of  $\Theta_{num}$ . Quantitatively,  $\alpha$  is twice as large as  $\Theta_{num}$  (not shown). At the second order, the asymptotic prediction agrees even less with  $\Theta_{num}$  than  $\alpha$  does. The gradient of the depth-averaged temperature for the SA solution is in

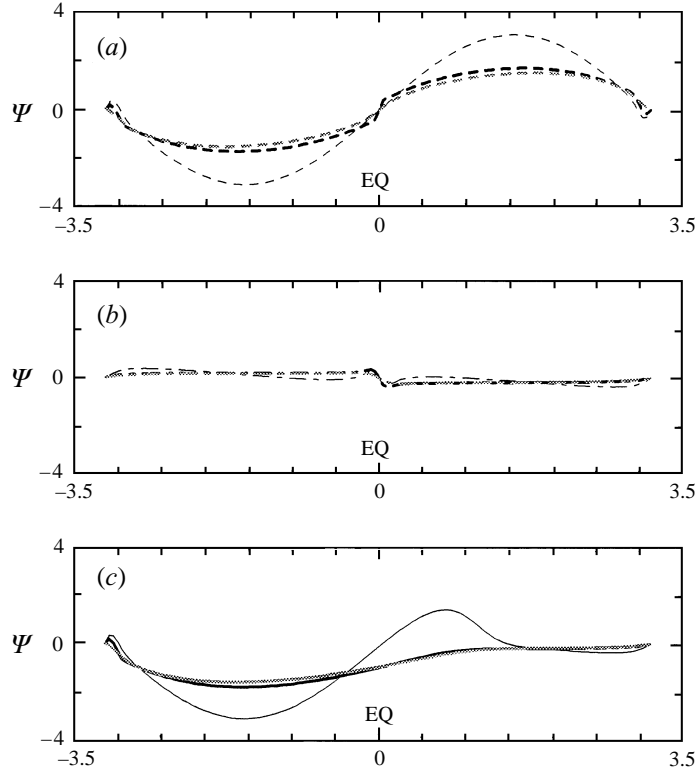


FIGURE 13. Depth-averaged streamfunctions for the *straight* forcing (FT1 and FS1) and the parameters  $a = 380$ ,  $b = 30$  and  $k = 0.2$ . Grey lines:  $\bar{\Psi}_{num}$ . Dark bold lines:  $\bar{\Psi}_1(\Sigma_{num}, \Theta_{num})$ . Dark thin lines:  $\bar{\Psi}_1(\Sigma_{num}, \alpha)$ . (a) TH solution. (b) SA solution. (c) PP solution.

good agreement with  $\alpha$  and in excellent agreement with the second-order asymptotic gradient of temperature. We note that the  $\Theta_{num}$  field exhibits stronger values in the SA circulation than in the TH circulation. Indeed, the streamfunction of the SA solution is very weak and  $\Theta_{num}$  is strongly dependent on the temperature forcing, while the stronger advection of the TH circulation tends to homogenize horizontally the temperature.

The comparison between the three depth-averaged streamfunctions  $\bar{\Psi}_{num}$ ,  $\bar{\Psi}_1(\Sigma_{num}, \Theta_{num})$  and  $\bar{\Psi}_1(\Sigma_{num}, \alpha)$  gives similar results to the *loop* case (see §5.2). The different fields are displayed in figure 13 for the three circulations displayed in figure 3.

Figure 14 presents the function  $\chi(\mathcal{Y}, \Theta_{num}, \Sigma_{num})/B_{max}$ , defined in equation (18) §3.3, for the three equilibria portrayed in figure 3. Here  $B_{max}$  is equal to  $b$ , the magnitude of the salinity forcing. The departures of  $\chi(\mathcal{Y}, \Theta_{num}, \Sigma_{num})/B_{max}$  from zero are less than 60% for the TH equilibria and less than 20% for the SA equilibria. In the latter case, both  $\Sigma_{num}$  and  $\Theta_{num}$  are close to the asymptotically predicted values; then  $\chi(\mathcal{Y}, \Theta_{num}, \Sigma_{num})$  almost vanishes, as required theoretically, except at the ‘pinching discontinuity’ (see §5.1).

The function  $\chi(\mathcal{Y}, \Theta_{num}, \Sigma_{num})$  is the sum of three horizontal fluxes of salinity, i.e.  $B$  due to the forcing,  $k^2\Sigma_{num}$  due to the diffusion and  $C^2(\Theta_{num} - \Sigma_{num})^2\Sigma_{num}$  due to the advection. These three components are displayed in figure 15 for each equilibrium in figure 3. The forcing flux is, of course, the same for the three circulations.

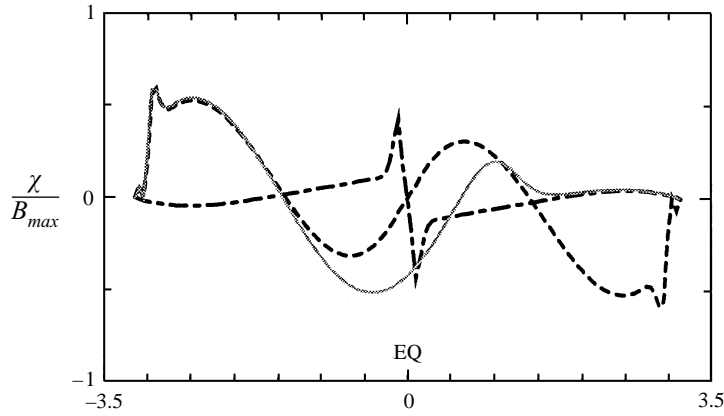


FIGURE 14. Function  $\chi[\mathcal{Y}, \Theta_{num}(y), \Sigma_{num}(y)]$  displayed following  $\mathcal{Y}$  in the *straight* case (FT1 and FS1) with  $a = 380$  with  $b = 30$  and  $k = 0.2$ . TH solution ( - - - - ), SA solution ( - · - · - ) and PP solution (grey solid line).

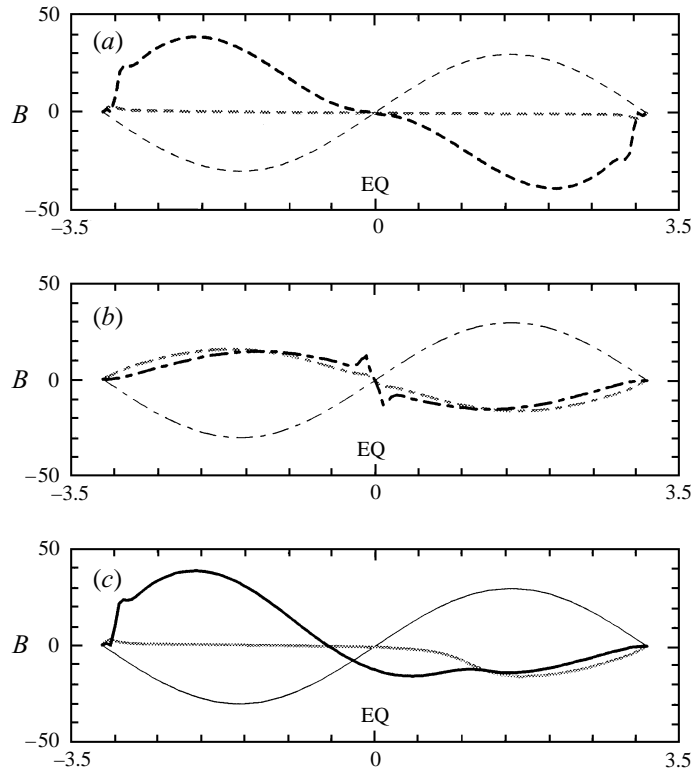


FIGURE 15. Three components of the function  $\chi(\mathcal{Y}, \Theta_{num}, \Sigma_{num})$  in the *straight* case (FT1 and FS1) with  $a = 380$ ,  $b = 30$  and  $k = 0.2$ . Thin lines: forcing salinity flux. Grey bold lines: diffusive salinity flux. Dark bold lines: advective salinity flux. (a) TH solution. (b) SA solution. (c) PP solution.

In the TH circulation, the diffusive flux (figure 15a, grey line) is almost equal to zero in the whole domain, just like  $\Sigma_{num}$ , and the advective flux (figure 15a, bold line) is opposite to and more important than the forcing flux (figure 15a, thin line), except close to the equator. The advection acts against the forcing, because it tends

to homogenize horizontally the salinity field ( $\Sigma_{num} \simeq 0$ ). The polar boundary layers are obvious in the advective component.

In the SA circulation, advective (figure 15b, bold line) and diffusive (figure 15b, grey line) fluxes are of similar importance and balance the forcing flux (figure 15b, thin line). The surface transport of salt through advection tends to fight the salinity forcing. The strong influence of the diffusive flux is obvious in the temperature and salinity fields (figure 3b), which are almost vertically homogeneous. This feature favours a stabilization of the water column and, thus, acts against the destabilizing influence of the salinity forcing at the equator.

It is interesting to look at the PP circulation and to observe that the ‘superposition principle’ is valid for both advective and diffusive fluxes, but that the connection between the SA and the TH components does not occur at the same location for both fluxes. The diffusive flux (figure 15c, grey line) of the PP solution is composed of the TH diffusive flux on more than one hemisphere and of the SA diffusive flux on two thirds of the other hemisphere. The boundary layer linking the two components is relatively thin. For the PP advective flux (figure 15c, bold line), a larger boundary layer develops across the equator, leading to a less extended TH component. The boundary layer is wider to connect the TH and SA advective fluxes, because they differ quantitatively more than the two diffusive fluxes. The linear diffusive term is easier to connect numerically than the advective term that is third order in  $\Sigma$ .

The numerical solutions (not shown) obtained with a lower aspect ratio ( $k = 0.1$ ) agree even better with the asymptotic predictions.  $\Sigma_{num}$  follows more closely the theoretical solutions, and the regions of boundary layers (TH and PP) or fronts (SA) are thinner. Fronts appear as Dirac functions of  $\Sigma_{num}$ . The function  $\chi(\mathcal{Y}, \Theta_{num}, \Sigma_{num})$  is confined to very smaller values (interval of fluctuations five times reduced compared to the case  $k = 0.2$ ). Numerical results with a lower aspect ratio than  $k = 0.1$  have not been obtained.

We can conclude the *straight* case by noticing that the quality of the asymptotic predictions is even more obvious here than in the *loop* case. The depth-averaged salinity  $\Sigma_{num}$  is almost equal to the theoretical solutions of the asymptotic equation, except on very thin belts of latitudes, where boundary layers develop. The agreement between theory and simulations becomes greater when the aspect ratio is decreased. Unfortunately, the temperature structure is not predicted correctly, except for the SA circulation, which is both the globally defined solution and the less intense one. In the SA numerical solution, an unpredicted front exists at the equator due to the pinching effect of downwelling, already mentioned in §5.1.

## 7. Numerical simulations in the *cubic* case (FT2 and FS1)

The numerical results observed in this case are displayed in figure 4 and the asymptotic solutions presented in figure 7(d). Figure 16 shows asymptotic and numerical solutions of  $\Sigma$ . Figure 17 presents similar curves for a forcing close to the present one, but *straight*.

### 7.1. Structure of the solutions

Applying the forcing profiles FT2 and FS1 and the parameters ( $a = 488$ ,  $b = 40$ ,  $k = 0.2$ ), three equilibria are numerically obtained, which are displayed in figure 4. The SA-type circulation (figure 4b) exhibits fronts at the lateral boundaries. Close to the poles, TH-type cells of circulation develop. Such a cell is observed also at one of the polar boundaries in the asymmetric circulation (figure 4c). Figure 16 shows

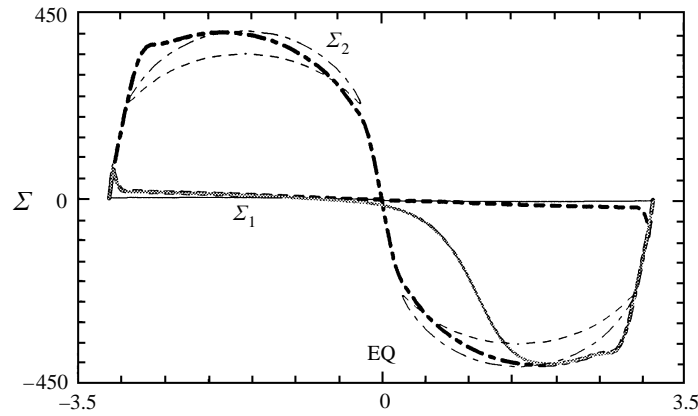


FIGURE 16.  $\Sigma(\mathcal{Y})$  with the *cubic* forcing (FT2 and FS1) and the parameters  $a = 488$ ,  $b = 40$  and  $k = 0.2$ . Theoretical solutions are thin lines: stable (——), metastable (— · — · —) and unstable (----) branches of solution. Numerical solutions are bold lines: TH (----), SA (— · — · —) and PP (grey solid line).

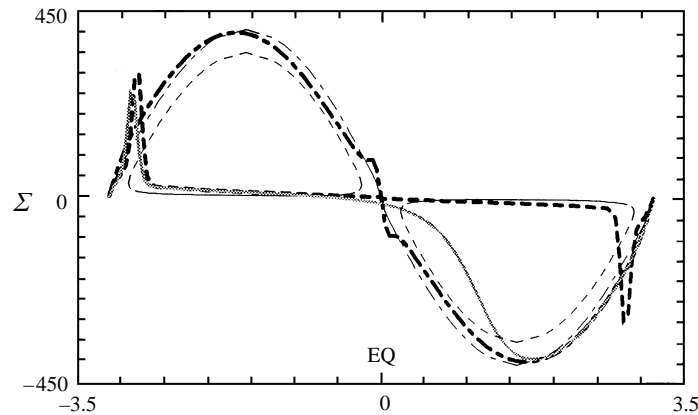


FIGURE 17.  $\Sigma(\mathcal{Y})$  with the *straight* forcing (FT1 and FS1) and the parameters  $a = 380$ ,  $b = 40$  and  $k = 0.2$ . Theoretical solutions are thin lines: stable (——), metastable (— · — · —) and unstable (----) branches of solution. Numerical solutions are bold lines: TH (----), SA (— · — · —) and PP (grey solid line).

the asymptotic solutions  $\Sigma$  with these forcing and parameters (thin lines) and  $\Sigma_{num}$  computed for the three observed equilibria (bold lines).

Here, the TH solution (figure 16, bold dashed line) corresponds to the asymptotic globally defined solution. But, close to the poles,  $\Sigma_{num}$  differs from the asymptotic solution. It evolves exactly as in the *straight* case (figure 11), where the TH starts like the global SA solution and jumps after to the local TH branch. This discrepancy between asymptotic and numerical solutions has no obvious explanation. It is as if the *cubic* case were feeling that it is close to the *straight* case in a sense that will be developed below.

The lateral fronts of the SA circulation (figure 4b) are clearly seen and the corresponding  $\Sigma_{num}$  (figure 16, bold dot-dashed line) exhibits a very sharp gradient close to the poles. The transition around the equator between the two local branches happens smoothly through a boundary layer.  $\Sigma_{num}$  is highly asymmetric with respect to the

mid-hemisphere. It exhibits stronger departures from the  $\Sigma_2$  theoretical solution than in any previous case of forcing.

Once again, the PP circulation (figure 4c and figure 16, grey solid line) is the juxtaposition of the TH solution in one hemisphere and of the SA equilibria in half of the other one, joined together by a large boundary layer.

### 7.2. Further validation of the asymptotic equations

The same diagnostics as in §5.2 have been applied to the numerical results. The conclusions are analogous to those obtained in the *straight* case and detailed in §6.3.

We just note that the shape of  $\Theta_{num}$  in the TH circulation is here correctly approximated by the  $\alpha$ -function (not shown), but its amplitude is half the size. For all the diagnostics concerning the TH circulation, numerical irregularities appear, which correspond to the polar front mentioned above. As previously, the best agreement between asymptotic predictions and numerical results is obtained for the SA-type circulation which is no longer the globally defined one. The agreement comes from the fact that this circulation is the less intense one. Simulations performed with a lower aspect ratio  $k = 0.05$  (not shown) indicate an improvement of the asymptotic predictions, even concerning the temperature related field  $\Theta_{num}$ .

We note that it is possible to obtain three equilibria without any counter-rotating cells at the lateral boundaries with the forcing profiles FT2 and FS1 by increasing the parameter  $b$  or by decreasing  $a$  (for example by using  $a = 488$ ,  $b = 90$  and  $k = 0.2$ ).

### 7.3. Comparison of the three forcings

We compare the results of figure 16, performed in the *cubic* case with  $T(y, 0) = 488 \times \text{FT2}(ky)$  and  $\partial S(y, 0)/\partial z = 40 \times \text{FS1}(ky)$ , with the ones of figure 17, obtained in the *straight* case with  $T(y, 0) = 380 \times \text{FT1}(ky)$  and the same salinity forcing. The two temperature forcings are displayed in figure 7(a) and look similar except in the vicinity of  $\sin(\mathcal{Y}) = 0$ .

With the *straight* forcing, three equilibria (not shown) are obtained. The salinity-driven circulation extends over the whole domain, while the thermally driven one exhibits counteracting cells delimited by stationary fronts close to the lateral boundaries. By looking at the geometric constructions portrayed in figure 7(c) (*straight*) and figure 7(d) (*cubic*), one can see that the numerical equilibrium extended over the whole domain corresponds, in both cases of forcing, to the asymptotic globally defined solution.

The comparison between the solutions  $\Sigma$  of the asymptotic equation and the  $\Sigma_{num}$  calculated for the three equilibria obtained with the *straight* forcing is presented in figure 17. The counter-rotating cells and the stationary fronts of the TH solution are obvious in the figure. The agreement between theory and simulations is better for the *straight* forcing than for the *cubic* one.

Let us note that a comparison between figure 11 and figure 17 reveals that a change in the surface forcing affects the solutions mostly in the vicinity of the latitudes such that  $\sin(\mathcal{Y}) = 0$ . Indeed, the corresponding simulations have been performed with the same surface forcing and parameters, except the salinity forcing magnitude which is equal to  $b = 30$  in figure 11 and to  $b = 40$  in figure 17. The solutions are almost unchanged, except at the equator and at the poles.

The similarity in the behaviour of the TH solutions underlines the proximity of the *cubic* and *straight* forcings. Even if the asymptotic topology of the solutions differs for the two cases, they are two unfoldings of a same degenerate situation, which would correspond to the  $k = 0$  limit of the asymptotic expansion with three globally

defined solutions. If  $k$  decreases faster than scaled in the expansion presented in §3 (for example  $k = \epsilon^2 k_2$ ), the asymptotic solutions must satisfy  $\chi_2 [y, \alpha(y), \Sigma(y)] = B(y) + C^2(\alpha - \Sigma)^2 \Sigma = \phi$ . The diffusive horizontal flux of salinity does not appear any longer in this equation. Thanks to this simplification of the problem, three equilibria defined in the whole box can be found for various choices of surface forcing (e.g. *cubic*) and a suitable domain in the  $(a, b)$ -plane. The theoretical domain where multiple equilibria exist is delimited by the horizontal axis and a *cubic* curve in the plane  $(a, b)$ . The topological structure of the asymptotic solutions  $\Sigma$  then looks like that presented in figures 7(c) and 7(d), but the three solutions meet at the equator and at the poles. In this case the ‘superposition principle’ is exactly verified in the formation of an asymmetric solution.

The *loop* forcing is a third unfolding of the same degenerate situation. This forcing seems rather different from the two other surface forcings, because it is not symmetric with respect to the mid-hemisphere. But, as in the *straight* and the *cubic* cases, multiple globally defined equilibria exist while they are not predicted by the asymptotic expansion. Comparing figures 5(c) to figure 7(c) and 7(d), one can easily see that the *loop* case is topologically close to the other forcings and comes from the same degenerate situation in the  $k = 0$  limit of the asymptotic expansion.

## 8. Conclusion

In this article, we have compared the numerical results obtained with a two-dimensional Boussinesq model of the thermohaline convection and the solutions of an asymptotic equation in the limit of a small aspect ratio. The validation of the asymptotic approach has been presented using three different surface forcing profiles. These forcings have been chosen in order to exhibit different dynamical behaviours, such as the formation of thermohaline fronts and the existence of multiple equilibria. For these forcings, called *loop*, *straight* and *cubic*, we have presented numerical results, asymptotic solutions, and comparisons between them.

The asymptotic analysis is found to be a very simple and powerful tool to predict the topology of the solutions. All the topological structures studied (*loop*, *straight*, *cubic*) appear to be unfoldings of a same degenerate situation where three equilibria are globally defined for a vanishing aspect ratio.

The asymptotic theory is only valid outside the boundary layers, which develop in the vicinity of the fronts connecting two different branches of solutions. A two-dimensional boundary layer analysis would be needed in order to compute the inner solutions. We have also observed discontinuities which are not described by the asymptotic equation. They correspond to a pinching of the streamlines similar to the narrowing of downwelling addressed in other studies (Stommel 1962).

Considering the results presented here, it makes sense to apply this approach to more complex models of the thermohaline circulation. The introduction of new parametrizations, such as surface momentum forcing or rotation, in a two-dimensional model could be tested through the asymptotic analysis. Moreover, the reduction of a three-dimensional fluid model to two-dimensional asymptotic equations can be addressed with this approach.

Since multiple equilibria and fronts are observed in a great variety of models, from the most idealized to the fully coupled climate models, it is of importance to understand the mechanisms generating them. While very crude in the context of realistic studies, the use of simple process models and the development of analytical

tools, such as the one validated here, are essential for a better understanding of these mechanisms.

This work was funded by the European Communities under contract MAST-CT92-0034. The authors are grateful to Paola Cessi for many fruitful scientific discussions.

#### REFERENCES

- BROECKER, W. S., PETEET, D. M. & RIND, D. 1985 Does the ocean-atmosphere system have more than one stable mode of operation. *Nature* **315**, 21–26.
- BRYAN, F. 1986 High-latitude salinity effects and interhemispheric thermohaline circulations. *Nature* **323**, 301–304.
- CESSI, P. & YOUNG, W. R. 1992 Multiple equilibria in two-dimensional thermohaline circulation. *J. Fluid Mech.* **241**, 291–309.
- DIJKSTRA, H. A. & MOLEMAKER, M. J. 1997 Symmetry breaking and overturning oscillations in thermohaline driven flows. *J. Fluid Mech.* **331**, 169–198.
- KENNETT, J. P. & STOTT, L. D. 1991 Abrupt deep-sea warming, palaeoceanographic changes and benthic extinctions at the end of the Palaeocene. *Nature* **353**, 225–229.
- MAIER-REIMER, E., MIKOLAJEWICZ, U. & HASSELMANN, K. 1993 Mean circulation of the Hamburg LSG OGCM and its sensitivity to the thermohaline surface forcing. *J. Phys. Oceanogr.* **23**, 731–757.
- MANABE, S. & STOUFFER, R. J. 1988 Two stable equilibria of a coupled ocean-atmosphere model. *J. Climate* **1**, 841–866.
- MAROTZKE, J. 1990 Instabilities and multiple equilibria of the thermohaline circulation. PhD Thesis, Christian Albrechts University of Kiel.
- MAROTZKE, J., WELANDER, P. & WILLEBRAND, J. 1988 Instability and multiple steady states in a meridional-plane of the thermohaline circulation. *Tellus* **40A**, 162–172.
- QUON, C. & GHIL, M. 1992 Multiple equilibria in thermosolutal convection due to salt-flux boundary conditions. *J. Fluid Mech.* **245**, 449–483.
- QUON, C. & GHIL, M. 1995 Multiple equilibria and stable oscillations in thermosolutal convection at small aspect ratio. *J. Fluid Mech.* **291**, 33–56.
- ROOTH, C. 1982 Hydrology and ocean circulation. *Prog. Oceanogr.* **11**, 131–149.
- STOMMEL, H. 1961 Thermohaline convection with two stable regimes of flow. *Tellus* **XIII-2**, 224–230.
- STOMMEL, H. 1962 On the smallness of sinking regions in the ocean. *Proc. Natl Acad. Sci. Washington* **48**, 766–772.
- THUAL, O. & MCWILLIAMS, J. C. 1992 The catastrophe structure of thermohaline convection in a two-dimensional fluid model and a comparison with low-order box models. *Geophys. Astrophys. Fluid Dyn.* **64**, 67–95.
- VELLINGA, M. 1996 Instability of two-dimensional thermohaline circulation. *J. Phys. Oceanogr.* **26**, 305–319.
- WELANDER, P. 1986 Thermohaline effects in the ocean circulation and related simple models. In *Large-Scale Transport Processes in Oceans and Atmosphere* (ed. J. Willebrand & D. T. L. Anderson), pp. 163–200. D. Reidel.
- WEAVER, A. J. & HUGHES, T. M. C. 1992 *Stability and Variability of the Thermohaline Circulation and its Link to Climate*. Trends in Physical Oceanography, Council of Scientific Research Integration - Research Trends Series, Trivandrum India.
- WEAVER, A. J., MAROTZKE, J., CUMMINS, P. F. & SARACHIK, E. S. 1993 Stability and variability of the thermohaline circulation. *J. Phys. Oceanogr.* **23**, 39–60.
- WINTON, M. & SARACHIK, E. S. 1993 Thermohaline oscillations induced by strong steady salinity forcing of ocean general circulation models. *J. Phys. Oceanogr.* **23**, 1389–1410.
- WRIGHT, D. G. & STOCKER, T. F. 1991 A zonally averaged ocean model for the thermohaline circulation. Part I: Model development and flow dynamics. *J. Phys. Oceanogr.* **21**, 1713–1724.